Mammalian HP1 Isoforms Have Specific Roles in Heterochromatin Structure and Organization

Laia Bosch-Presegué, Helena Raurell-Vila, Joshua K. Thackray, Jessica González, Carmen Casal, Noriko Kane-Goldsmith, Miguel Vizoso, Jeremy P. Brown, Antonio Gómez, Juan Ausió, Timo Zimmermann, Manel Esteller, Gunnar Schotta, Prim B. Singh, Lourdes Serrano, Alejandro Vaquero

November 2017

Cell Reports

Mammalian HP1 Isoforms Have Specific Roles in Heterochromatin Structure and Organization

Graphical Abstract

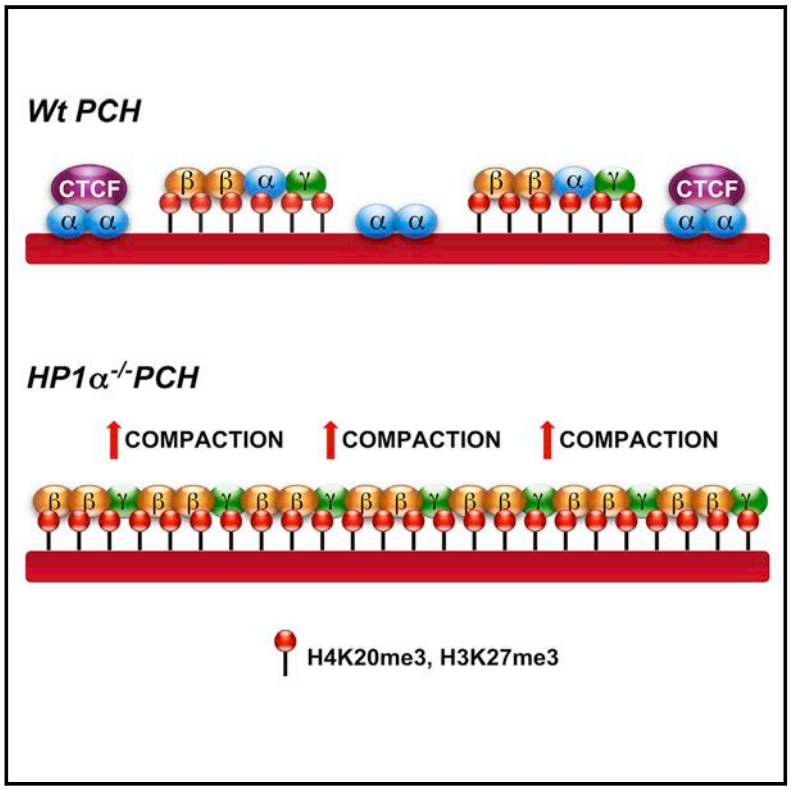

Authors

Laia Bosch-Presegué,
Helena Raurell-Vila,
Joshua K. Thackray, ..., Prim B. Singh,
Lourdes Serrano, Alejandro Vaquero

Correspondence

avaquero@idibell.cat

In Brief

Bosch-Presegué et al. find that HP1a interacts with CTCF in pericentric heterochromatin (PCH) and restricts H4K20me3 and H3K27me3 distribution. Loss of HP1a results in PCH hypercompaction and a distinctive pattern of mitotic defects. HP1b is functionally related to H4K20me3 deposition and inhibits CTCF distribution, and its deficiency produces decompaction of PCH.

Highlights

- HP1a plays a unique role in heterochromatin organization and structure
- HP1a interacts with CTCF and confines H4K20me3 and H3K27me3 to PCH foci
- Loss of HP1a, but not HP1b and HP1g, induces global hypercompaction of chromatin
- HP1b is functionally associated with H4K20me3

Bosch-Presegué et al., 2017, Cell Reports *21*, 2048–2057
November 21, 2017
https://doi.org/10.1016/j.celrep.2017.10.092

CellPress

OPEN ACCESS
CellPress

Cell Reports
Report

Mammalian HP1 Isoforms Have Specific Roles in Heterochromatin Structure and Organization

Laia Bosch-Presegué,[1,2,12] Helena Raurell-Vila,[1,12] Joshua K. Thackray,[3] Jessica González,[1] Carmen Casal,[4] Noriko Kane-Goldsmith,[3] Miguel Vizoso,[5] Jeremy P. Brown,[6] Antonio Gómez,[7] Juan Ausió,[8] Timo Zimmermann,[9] Manel Esteller,[5] Gunnar Schotta,[10] Prim B. Singh,[6,11] Lourdes Serrano,[3] and Alejandro Vaquero[1,13,*]

[1]Chromatin Biology Laboratory, Cancer Epigenetics and Biology Program (PEBC), Institut d'Investigació Biomèdica de Bellvitge (IDIBELL), Av. Gran Via de l'Hospitalet, 199-203, 08907- L'Hospitalet de Llobregat, Barcelona, Spain
[2]Tissue Repair and Regeneration Group, Department of Biosciences, Universitat de Vic, Universitat Central de Catalunya, Vic, Spain
[3]Department of Genetics, Human Genetics Institute, Rutgers University, 145 Bevier Road, Piscataway, NJ 08854, USA
[4]Microcopy Unit, Institut d'Investigació Biomèdica de Bellvitge (IDIBELL), Av. Gran Via de l'Hospitalet, 199-203, 08908- L'Hospitalet de Llobregat, Barcelona, Spain
[5]Cancer Epigenetics Laboratory, Cancer Epigenetics and Biology Program (PEBC), Institut d'Investigació Biomèdica de Bellvitge (IDIBELL), Av. Gran Via de l'Hospitalet, 199-203, 08908- L'Hospitalet de Llobregat, Barcelona, Spain
[6]Fächerverbund Anatomie, Institut für Zell-und Neurobiologie, Charite-Universitätsmedizin, 10117 Berlin, Germany
[7]Centre for Genomic Regulation (CRG), The Barcelona Institute of Science and Technology, Dr. Aiguader 88, Barcelona 08003, Spain
[8]Center for Biomedical Research, University of Victoria, Victoria, BC V8W 3N5, Canada
[9]Advanced Light Microscopy Unit, Center for Genomic Regulation, C/ Dr. Aiguader 88, 08003 Barcelona, Spain
[10]Ludwig Maximilians University and Munich Center for Integrated Protein Science (CiPSM), Biomedical Center, Planegg-Martinsried, Germany
[11]Department of Biomedical Sciences, Nazarbayev University School of Medicine, Astana 010000, Republic of Kazakhstan
[12]These authors contributed equally
[13]Lead Contact
*Correspondence: avaquero@idibell.cat
https://doi.org/10.1016/j.celrep.2017.10.092

SUMMARY

HP1 is a structural component of heterochromatin. Mammalian HP1 isoforms HP1α, HP1β, and HP1γ play different roles in genome stability, but their precise role in heterochromatin structure is unclear. Analysis of *Hp1α*$^{-/-}$, *Hp1β*$^{-/-}$, and *Hp1γ*$^{-/-}$ MEFs show that HP1 proteins have both redundant and unique functions within pericentric heterochromatin (PCH) and also act globally throughout the genome. HP1α confines H4K20me3 and H3K27me3 to regions within PCH, while its absence results in a global hyper-compaction of chromatin associated with a specific pattern of mitotic defects. In contrast, HP1β is functionally associated with Suv4-20h2 and H4K20me3, and its loss induces global chromatin decompaction and an abnormal enrichment of CTCF in PCH and other genomic regions. Our work provides insight into the roles of HP1 proteins in heterochromatin structure and genome stability.

INTRODUCTION

The alteration of pericentric heterochromatin (PCH) organization and structure have been linked to cell-cycle-progression defects, DNA damage, chromosomal aberrations, apoptosis, cancer, and aging (Benayoun et al., 2015; Carone and Lawrence, 2013). PCH is defined by several features including specific histone modifications, structural proteins, histone variants, DNA hypermethylation, and an undefined RNA component (Saksouk et al., 2015). Two histone marks, H3K9me3 and H4K20me3, have been proposed as being hallmarks of PCH structure (Rea et al., 2000; Schotta et al., 2004).

H3K9me3 is mainly catalyzed by the histone methyltransferase Suv39h1 and its close relative Suv39h2 and functions as a docking site for specific factors (Bannister et al., 2001; Lachner et al., 2001), whereas H4K20me3 is catalyzed by Su(var)4-20h2 and is directly involved in chromatin compaction and cohesin recruitment (Hahn et al., 2013). How these marks are distributed throughout heterochromatin and whether they co-localize in the same regions within heterochromatic regions are currently unknown. A key factor in heterochromatin structure is heterochromatin protein 1 (HP1), which was originally described in *Drosophila* as a suppressor of position-effect variegation (Eissenberg et al., 1990). Mammals harbor three HP1 isotypes termed HP1α, HP1β, and HP1γ (Jones et al., 2000). A growing body of evidence suggests that the role of HP1 proteins in genome stability goes beyond heterochromatin structure as they play a role in gene expression, DNA replication, DNA repair, cell cycle, cell differentiation, and development (Maison and Almouzni, 2004). All three isoforms localize to PCH although HP1β and HP1γ are also found in euchromatic regions (Maison and Almouzni, 2004). HP1 proteins participate in the establishment and propagation of the heterochromatin structure through their specific binding both to H3K9me3 and Suv39h1 (Bannister et al., 2001; Lachner et al., 2001). In this sense, HP1β was suggested to act as a bridge between H3K9me3-enriched chromatin fibers (Hiragami-Hamada et al., 2016). Interestingly, recent studies have suggested that HP1-mediated compaction also involves phase separation from soluble chromatin (Larson

et al., 2017; Strom et al., 2017). HP1 proteins also act as adapter molecules that link other factors to heterochromatin such as Suv4-20h2 or DNA methyltransferases among others (Fuks et al., 2003; Hahn et al., 2013).

Despite these advances, the question remains as to the relative contributions of each of HP1 isotype to heterochromatin organization and structure. This inquiry has been hampered by the strong functional redundancy of HP1 proteins, the abundance of all three isoforms in PCH foci, and their ability to homo- and hetero-dimerize (Canzio et al., 2014). Thus, the role of the three isoforms in heterochromatin has been considered to be more or less equivalent. However, the fact that the three isoforms have a distinct pattern of genomic distribution, specific interaction partners, and post-translational modifications, suggests that they likely perform different functions in cell physiology (Kwon and Workman, 2011; Maison and Almouzni, 2004). This possibility has been supported by recent evidence showing a more direct role of HP1α and HP1γ in Suv39h1 function in PCH than in HP1β (Raurell-Vila et al., 2017). Furthermore, mutational analyses have shown tissue-specific phenotypes in HP1α, HP1β, and HP1γ knockout (KO) mice (Aucott et al., 2008; Brown et al., 2010; Maksakova et al., 2011; Singh, 2010).

The functional differences between HP1α and HP1β are particularly relevant as both isoforms are enriched within PCH and their combined loss abrogates HP1γ localization in these regions (Dialynas et al., 2007). Aiming to understand the specific role of HP1α and HP1β isoforms in PCH, we analyzed the impact of each isoform on heterochromatin structure and organization using mouse embryonic fibroblast (MEF) cells derived from KO mice. Our studies suggest that HP1α plays a key role as an organizer of constitutive heterochromatin regions. Loss of HP1α results in the enrichment of H4K20me3 and H4K27me3 in PCH foci, whereas HP1β mediates a direct functional link with H4K20me3 and Suv420h2. Consistent with non-overlapping roles in PCH organization and structure, each mutant isoform exhibits a different pattern of H4K20me3 and H3K27me3 distribution in PCH that is associated with different types of mitotic aberrations. Our studies also suggest that HP1α and HP1β play opposite roles in CTCF distribution in PCH and other genomic regions. These studies provide insight into the specific roles of HP1 isoforms in heterochromatin structure.

RESULTS

Previous studies have suggested that the localization of endogenous HP1α and HP1β in PCH was broadly co-incident but not complete (Dialynas et al., 2007). We first aimed to confirm that the pattern of distribution of all three isoforms in PCH foci of NIH 3T3 cells is different. We expressed fluorescence-tagged HP1 isoforms and performed spectral imaging in PCH, which enabled us to correlate the intensity distribution of each isoform (Figure 1A, upper) and their relative localization relative to the foci center or radial position (Figure 1A, lower). As shown in Figures 1A and S1A–S1C, HP1α and HP1β are enriched in similar regions of PCH, preferentially toward the center of the foci. However, the intensity distribution was not identical, thereby suggesting a distinctive enrichment of both isoforms in PCH structure. HP1γ showed a lower degree of correlation with the other two isoforms with a rather more dispersed distribution within the foci (Figure 1A). Moreover, the loss of either HP1α or HP1β did not alter each other's levels in PCH but did induce an enrichment of HP1γ, suggesting that it plays an auxiliary role for both isoforms (Figures S1E and S1F) as has been previously suggested (Raurell-Vila et al., 2017). The interplay between the isotypes is also confirmed by the loss of HP1γ deposition in PCH upon simultaneous loss of HP1α and HP1β (Figure S1D), which has been seen previously (Dialynas et al., 2007).

HP1α Loss Induces H4K20me3 and H3K27me3 Enrichment in PCH Foci

We first analyzed the histone-modification changes in PCH foci that are associated with the specific loss of each HP1 isoform. To consider the possibility of cell-cycle-dependent events, we performed the analysis at different stages of the cell cycle. A loss of each HP1 isoform was correlated with a small decrease in H3K9me3 and a significant increase (1.5- to 1.7-fold) in H3K4me3 levels in PCH foci at all stages of the cell cycle (Figures 1B and S2A), thereby confirming that they are redundant with regard to the deposition of these histone modifications. There was also no significant impact on the DNA methylation levels at major satellite sequences between HP1α and the other isoforms (Figures S2B and S2C). In stark contrast, a loss of HP1α, but not of HP1β or HP1γ, resulted in a significant enrichment of H4K20me3 (around 1.8-fold) and H3K27me3 (around 2-fold) in the PCH foci during all cell-cycle stages (Figures 1B and S2A). Notably, increased levels of H4K20me3 were also observed at other genomic regions as well as the PCH (Figures S2A and S2D). Chromatin-immunoprecipitation (ChIP) assays confirmed that both H4K20me3 and H3K27me3 were increased in the major satellites of $Hp1\alpha^{-/-}$ MEFs compared to wild-type (WT) cells, while they were decreased in $Hp1\beta^{-/-}$ and $Hp1\gamma^{-/-}$ cells (Figure 1C).

To confirm that the changes in both marks were directly dependent on HP1α, we overexpressed Cre recombinase (R1) in $Hp1\alpha^{-/-}$ MEFs, which excised the promoter-trap Neo cassette that was used to generate the KO and restored HP1α gene integrity and expression (noKO) (Figure 2A). As expected, the re-expression of endogenous HP1α by the nuclease-driven removal of the Neo cassette (Figures 2B, S3A, and S3B) restored the levels of both marks in PCH foci. An identical result was obtained upon the overexpression of ectopic HP1α in $Hp1\alpha^{-/-}$ MEFs, demonstrating a direct role of HP1α in the control of these marks (Figures 2C and S3C). Interestingly, the re-deletion of HP1α (reKO) in noKO cells by FLP recombinase (R2) restored H3K27me3 levels but did not alter H4K20me3 (Figures 2B and S3B). The reKO generated a short-truncated form of HP1α (Figure S3A). To rule out any potential effect of the HP1α short-truncated form on H4K20me3, we knocked down HP1α by short hairpin RNA (shRNA) in NIH 3T3 cells. Consistently, HP1α loss resulted in H3K27me3 enrichment in PCH foci (1.6-fold) and no significant increase in H4K20me3 (Figures 2D, S3D, and S3E) (Hahn et al., 2013), suggesting a different deposition mechanism in PCH for both marks. We also knocked down HP1β and observed, in all cell-cycle stages except for G_2/M, a decrease in both H3K27me3 (25% reduction) and H4K20me3 (20% reduction) in PCH foci, supporting a direct role for HP1β in H4K20me3 deposition (Figures 2D, S3D, and S3E), which prompted us to

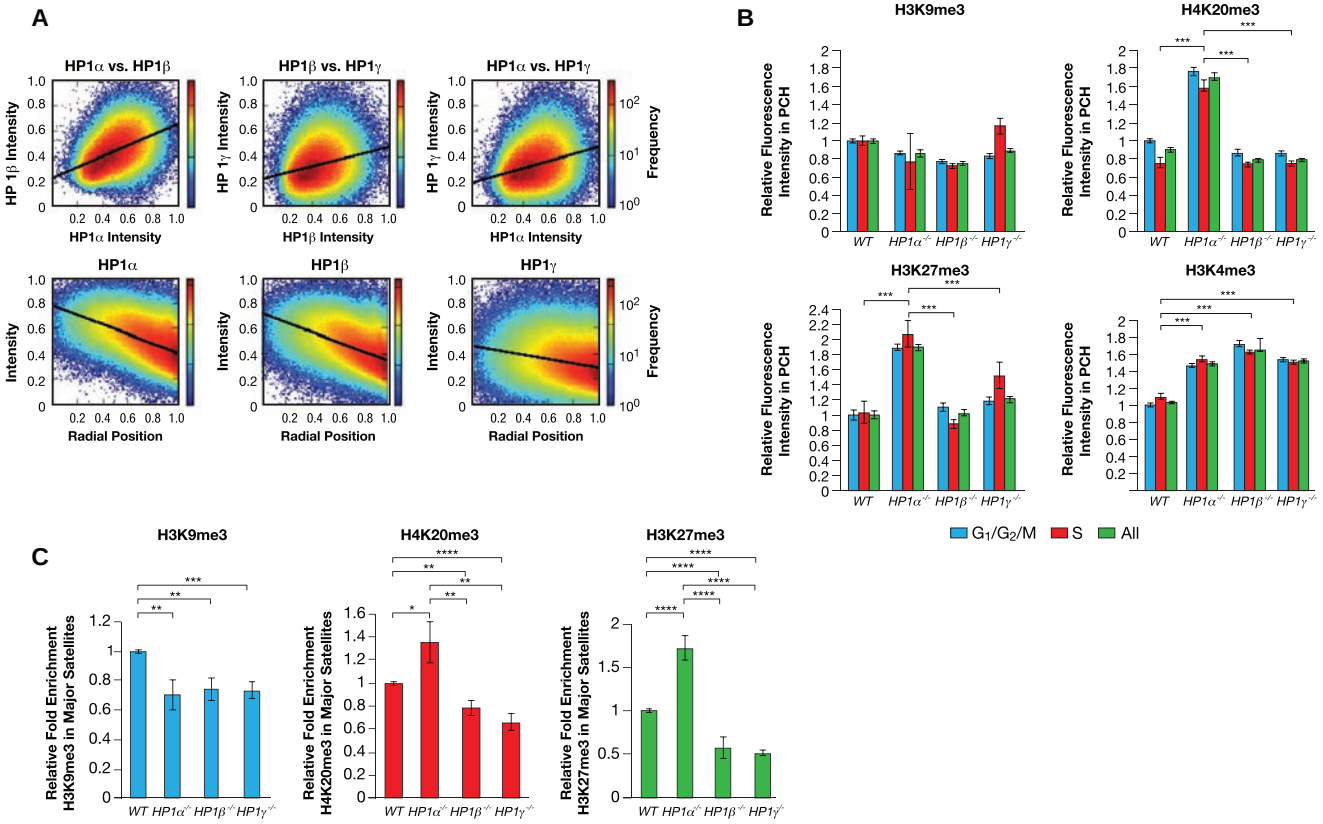

Figure 1. Loss of HP1α Induces H4K20me3 and H3K27me3 in PCH Foci

(A) 2D histograms showing HP1-isoform-distribution intensities in cells co-expressing all three HP1 isoforms. Colors represent the observed frequency on a logarithmic scale, and black lines shows the linear regression of the data points. Pairwise-intensity comparisons between indicated isoforms (top) and each HP1-isoform intensity plotted against the radial position are indicated with a value from 0 (chromocenter center) to 1 (periphery). Representative images are shown in Figure S1A. Intensity correlations quantified by Spearman rank-order correlation and linear least-squares regression are included in Figures S1B and S1C.

(B) Mean intensities of histone marks in the PCH foci from WT cells or MEFs *Hp1α*$^{-/-}$, *Hp1β*$^{-/-}$, and *Hp1γ*$^{-/-}$ through the different stages of the cell cycle. Representative images are shown in Figure S2A. ***p < 0.001.

(C) ChIP of H3K9me3, H4K20me3, and H3K27me3 in major satellites of indicated MEFs. *p < 0.05, **p < 0.01, ***p < 0.001, ****p < 0.0001.

explore the relationship between HP1β and H4K20me3 in more detail.

HP1β Is Functionally Linked to H4K20me3 and Suv420h2

Previous studies with recombinant HP1 proteins have suggested that all three isoforms may be equivalent in the regulation of H4K20me3 (Hahn et al., 2013). Interestingly, although we confirmed that all three isotypes interacted equally well with the Suv420h2 in nuclear soluble fractions of the transfected cells (data not shown), we observed a specific interaction between Suv420h2 and HP1β compared to the other isoforms in extracts enriched in digested insoluble chromatin upon highly stringent conditions (Figure 3A). Fluorescence resonance energy transfer (FRET) experiments confirmed these observations *in vivo* with a preferential binding of Suv420h2 to HP1β compared to HP1α and HP1γ (Figures 3B, S4A, and S4C). However, a fluorescence recovery after a photobleaching (FRAP) analysis of the dynamics of Suv420h2 in PCH foci of the WT, *Hp1α*-, *Hp1β*-, or *Hp1γ*-deficient MEFs showed a more complex picture. The loss of HP1β resulted in a decreased turnover of Suv420h2 at PCH and did not alter the Suv420h2 mobile fraction, whereas the loss of HP1α resulted in increased turnover of Suv420h2 in PCH compared to WT (Figures 3C and 3D). The overexpression of HP1α and HP1β had a small effect on the Suv420h2 residence time (Figures 3D and S4D). The decreased turnover upon HP1β loss contrasted with the increase turnover that was observed in HP1α-deficient cells, indicating an antagonistic role of HP1α and HP1β in Suv420h2 dynamics. Notably, HP1γ loss on Suv420h2 dynamics induced an effect between HP1α and HP1β, but its overexpression decreased its mobile fraction (Figures 3D and S4D). These FRAP analyses suggest that each isoform alters Suv420h2 dynamics in PCH in an isoform-specific manner. Taking our results together, we suggest that the effect of HP1β is likely to have a more direct role in Suv420h2 dynamics. A functional link between HP1β/Suv420h2 might also explain the decreased levels of H4K20me3 that were observed in both *Hp1β*$^{-/-}$ MEFs (Figure 1C) and upon shRNA-driven HP1β knockdown (Figure 2D). To obtain biochemical support for such an interaction, we undertook hemagglutinin (HA)

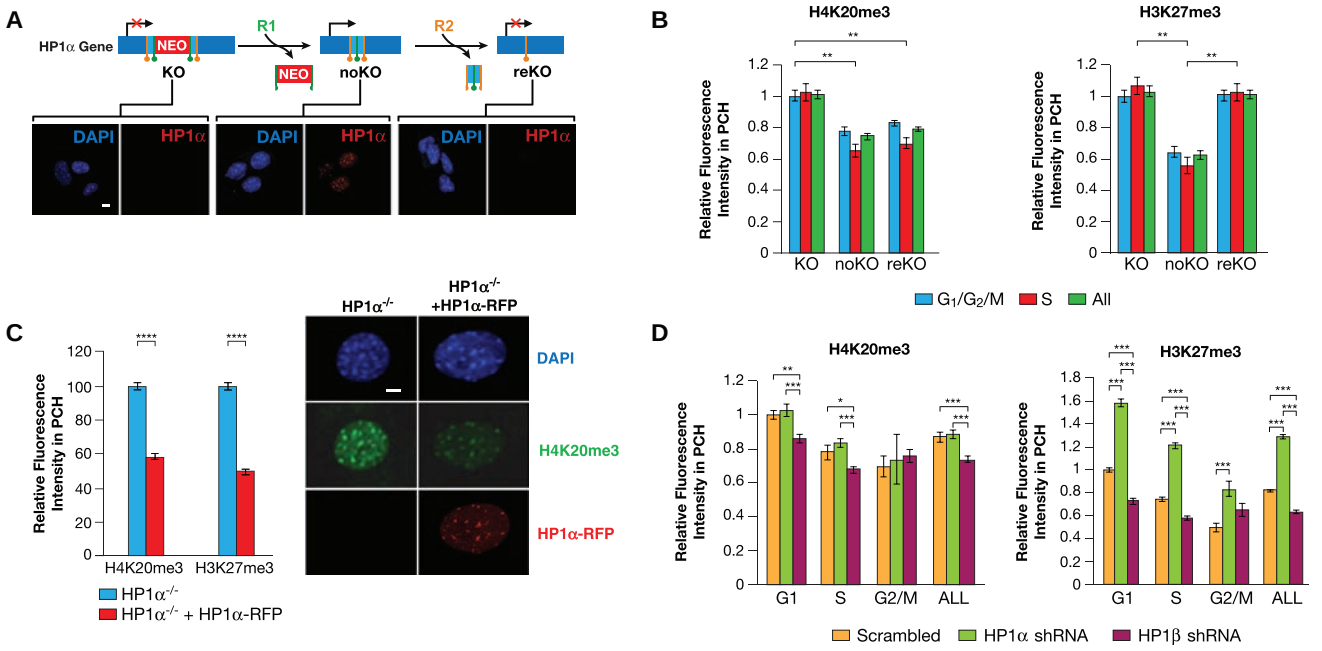

Figure 2. HP1α Directly Regulates H4K20me3 and H3K27me3 Enrichment in PCH Structure

(A) Generation of noKO and reKO cells from *Hp1α*$^{-/-}$ MEFs. HP1α protein levels were determined by IF and western blot (Figure S3A).

(B) Quantification of relative fluorescence intensity levels of H4K20me3 and H3K27me3 in HP1α KO, noKO, and reKO cells through the cell cycle. Representative images are shown in Figure S3B. **p < 0.01.

(C) Relative fluorescence intensity levels of H4K20me3 and H3K27me3 in PCH of KO cells upon ectopic expression of either an empty vector or HP1α-RFP. Representative images of H4K20me3 (right) and H3K27me3 (Figure S3C) are shown. ****p < 0.0001.

(D) Quantification, as in (B), of H4K20me3 and H3K27me3 levels in PCH of NIH 3T3 cells depleted in HP1α or HP1β by shRNA throughout the cell cycle (Figures S3D and S3E). *p < 0.05, ***p < 0.001.

affinity purification of HA-tagged HP1 isoforms, which showed that HP1β-containing chromatin was 1.5-fold enriched in H4K20me3 compared to HP1α or HP1γ, whereas H3K9me3 was detected at similar levels with all three isoforms (Figures 3E and S4E). We next tested the ability of each isoform to bind to H4K20me3 compared to H3K9me3 in peptide pull-downs using nuclear fractions containing HA-tagged HP1 isoforms (see Experimental Procedures). We performed these pull-downs under two different buffer conditions, the classical mild Dignam buffer and the highly stringent radioimmunoprecipitation assay (RIPA) buffer. We observed that all three isoforms bound strongly to H3K9me3-methylated peptide, but only HP1β bound to H4K20me3 resin (Figure 3F, Dignam). The binding of HP1β to H4K20me3 was more labile than to H3K9me3 because it was abrogated under very stringent RIPA conditions (Figure 3F, RIPA). These results suggested that, despite a strong redundancy between isoforms, HP1β binds to H4K20me3 with higher affinity than do the other isoforms. Consistently, re-ChIP experiments of endogenous HP1 isoforms (first ChIP) and H3K9me3 or H4K20me3 (second ChIP) of major satellites showed that the ratio H4K20me3/H3K9me3 in HP1β re-ChIP was clearly higher (1.25) than in HP1α (1) and HP1γ (0.3) (Figure 3G). This increased co-localization between HP1β and H4K20me3 was not an exclusive feature of PCH since a genome-wide analysis of previously reported ChIP sequencing (ChIP-seq) experiments in mouse embryonic stem cells (ESCs) confirmed a stronger overall correlation between HP1β and H4K20me3 compared to HP1α (Figure 3H).

CTCF Cooperates with HP1α in PCH Organization

Both Suv420h2 and H4K20me3 have been linked to cohesin enrichment in PCH (Hahn et al., 2013). We next tested whether the changes in H4K20me3 in *Hp1α*$^{-/-}$ MEFs also alter cohesin enrichment in PCH. ChIP experiments showed a 2-fold increase in cohesin levels at PCH in *Hp1β*$^{-/-}$ MEFs in contrast to *Hp1α*$^{-/-}$ and *Hp1γ*$^{-/-}$ (Figure 4A). This result suggested that HP1β may have an inhibitory effect on the accumulation of cohesins in PCH and that this enrichment was not associated to H4K20me3 levels. Cohesin distribution has been directly linked to CTCF, which is a major player in global genomic architecture (Cuddapah et al., 2009; Rubio et al., 2008). This link and the reported link of CTCF to PCH (Mukhopadhyay et al., 2004; Xiao et al., 2015) as well as HP1α (Agirre et al., 2015), led us to hypothesize that the H4K20me3-independent cohesin enrichment in *Hp1β*$^{-/-}$ MEFs may be related to abnormal levels of CTCF in PCH. Accordingly, we observed that, although the levels of CTCF in major satellites seem to be under the detection limit of ChIP in WT, *Hp1α*$^{-/-}$, and *Hp1γ*$^{-/-}$ cells, we did detect a significant enrichment (>7-fold) of CTCF in *Hp1β*$^{-/-}$ MEFs (Figure 4B). In contrast, no CTCF enrichment was detected in minor satellites (Figure 4B). Although CTCF was not detected in PCH by ChIP analysis, a detailed co-localization analysis of the endogenous CTCF signal within PCH confirmed the presence of CTCF in these regions (Figure S5B). These data are consistent with previous reports (Mukhopadhyay et al., 2004; Xiao et al., 2015) and indicate that CTCF is present in these regions either in limiting

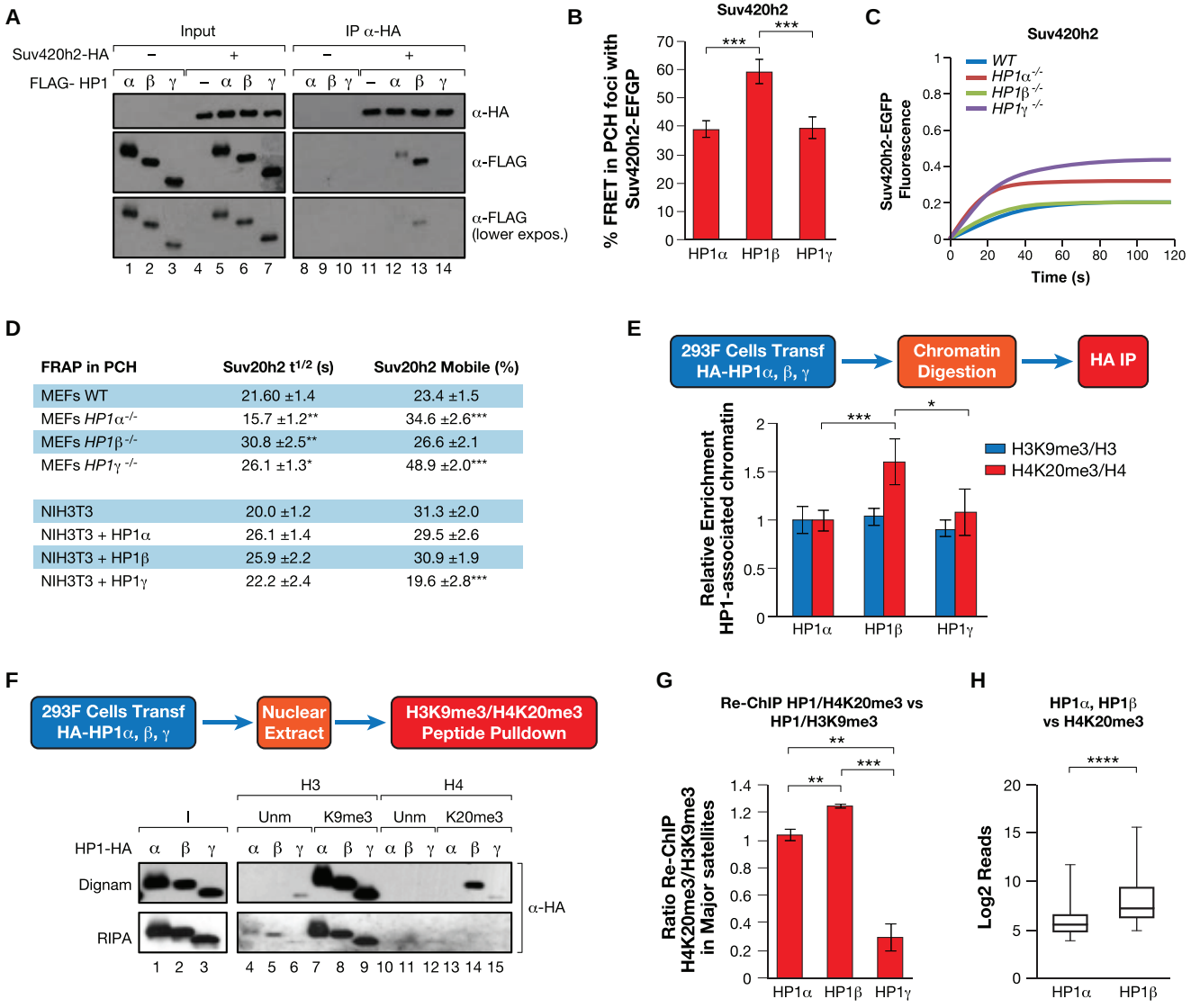

FRAP in PCH	Suv20h2 $t^{1/2}$ (s)	Suv20h2 Mobile (%)
MEFs WT	21.60 ±1.4	23.4 ±1.5
MEFs *HP1α*$^{-/-}$	15.7 ±1.2**	34.6 ±2.6***
MEFs *HP1β*$^{-/-}$	30.8 ±2.5**	26.6 ±2.1
MEFs *HP1γ*$^{-/-}$	26.1 ±1.3*	48.9 ±2.0***
NIH3T3	20.0 ±1.2	31.3 ±2.0
NIH3T3 + HP1α	26.1 ±1.4	29.5 ±2.6
NIH3T3 + HP1β	25.9 ±2.2	30.9 ±1.9
NIH3T3 + HP1γ	22.2 ±2.4	19.6 ±2.8***

Figure 3. HP1β Is Functionally Linked to Suv420h2 and H4K20me3

(A) Interaction between HA-HP1 isoforms and Suv420h2 in HEK293F cells using HA resin. Inputs (I) and elutions (E) are shown.

(B) Relative quantification of FRET analysis analyzing the interaction between HP1 isoforms (RFP) and Suv420h2 (GFP) in PCH foci of NIH 3T3 cells (Figure S4C) ***$p < 0.001$. FRET analysis controls are shown in Figures S4A and S4B.

(C) Relative fluorescence intensity of the FRAP assay in PCH foci for Suv420h2-EGFP in WT and HP1 KO cells.

(D) Quantification and statistical analysis of the FRAP experiment in (C) and FRAP in NIH 3T3 cells overexpressing HP1 isoforms (Figure S4D) such as the mobile fraction (Mobile [%]), and half-time of fluorescence recovery ($t^{1/2}$). *$p < 0.05$, **$p < 0.01$, ***$p < 0.001$.

(E) H3K9me3/H3 and H4K20me3/H4 levels in affinity purification of HA-tagged HP1 isoforms. Upper: schematic diagram of the experiment. Chromatin fractions of HEK293F cells expressing HA-tagged HP1 isoforms were digested with Benzonase and affinity purified with HA resin. Levels of H3K9me3 and H4K20me3 were normalized with histones H3 and H4, respectively, and the ratios in HP1β and γ pull-downs were quantified (n = 3) and represented relative to HP1α. A representative experiment is shown in Figure S4E. *$p < 0.05$, ***$p < 0.001$.

(F) Pull-down of HA-tagged HP1 isoforms with H3 or H4 (unmodified or H4K20me3)-biotinylated-streptavidin-agarose performed with HEK293F cell extracts generated in mild (Dignam) or stringent (RIPA) conditions.

(G) Re-ChIP experiments (n = 3) of endogenous HP1 isoforms (ChIP #1) and H3K9me3 or H4K20me3 (ChIP #2) in major satellites of NIH 3T3 cells. The ratio H4K20me3/H3K9me3 is shown for each isoform. **$p < 0.01$, ***$p < 0.001$.

(H) Correlation of the genome-wide co-localization between H4K20me3 and HP1α or HP1β in mouse ESCs. Boxplot of the log reads of H4K20me3 in the regions occupied by HP1α and HP1β based on previously published ChIP-seq experiments. ****$p < 0.0001$.

levels or under very specific conditions. Prompted by these data, we tested whether CTCF interacts with any of the HP1 isoforms *in vitro* and *in vivo*. We found that CTCF bound specifically to HP1α in immunoprecipitation experiments (Figure 4D). This result was supported by FRET as the FRET levels between HP1α and CTCF were 2-fold higher than for HP1β (Figures 4E

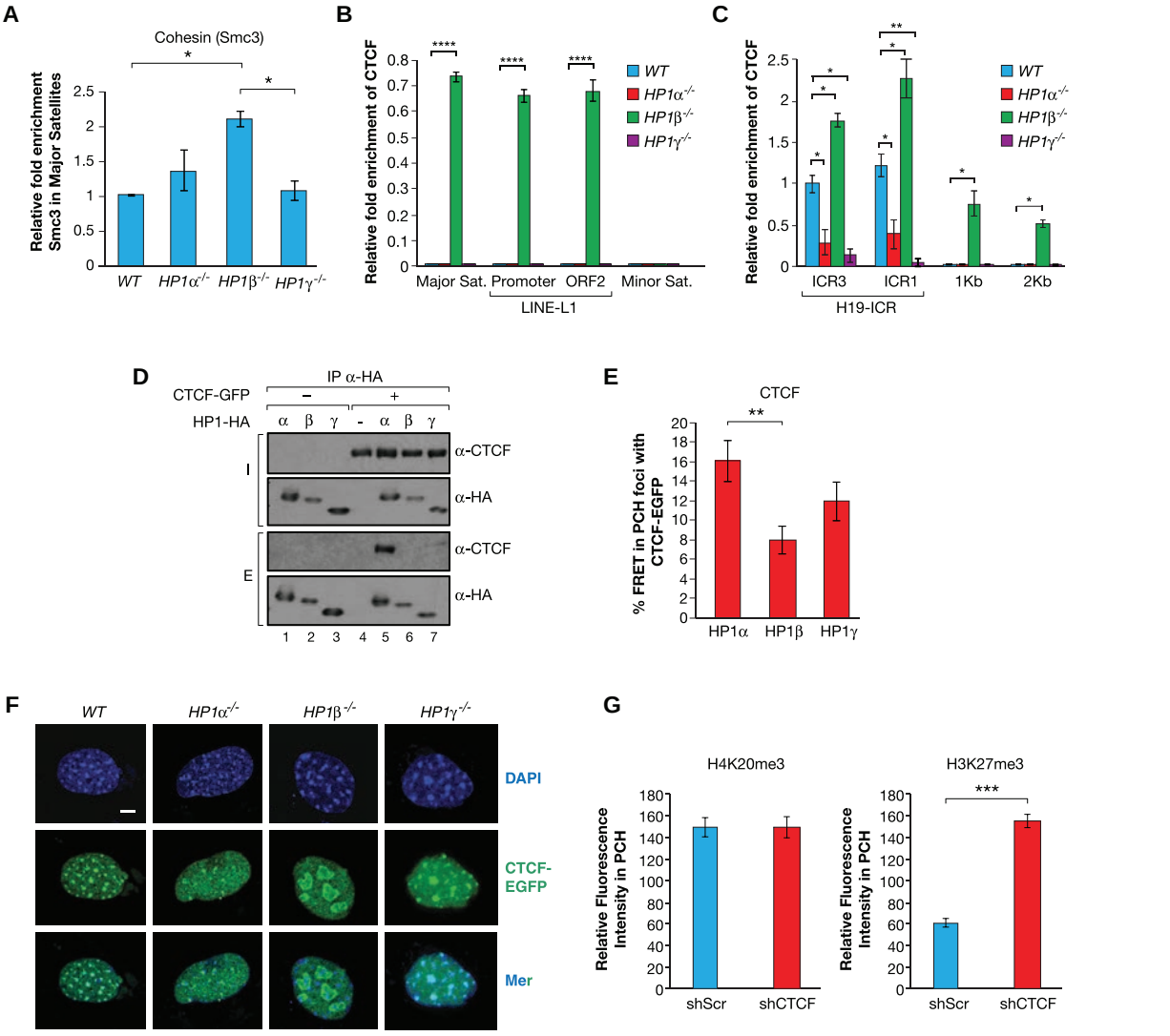

Figure 4. CTCF Plays a Role in HP1α-Dependent Regulation of PCH Organization

(A) ChIP of cohesin subunit Smc3 in Major satellites of the indicated MEFs. *p < 0.05.

(B) Representative ChIP (n = 3) of CTCF in major satellites, LINE-L1's promoter, and ORF2 and minor satellites in indicated MEFs. CTCF enrichment is represented relative to CTCF levels in H19-ICR of WT cells shown in (C). ****p < 0.0001.

(C). CTCF ChIP, as in (B), of H19-ICR CTCF binding sites ICR3 and ICR1 as well as 1 and 2 kb downstream of ICR1. *p < 0.001, **p < 0.005.

(D) HA immunoprecipitation of HEK293F extracts expressing HA-tagged HP1 isoforms, CTCF-EGFP, or both. Inputs and elutions are shown.

(E) FRET-acceptor photobleaching in PCH foci of NIH 3T3 cells between CTCF-EGFP and HP1-RFP isoforms (Figure S5A). **p < 0.01.

(F) CTCF-EGFP distribution in the nucleus of *WT* of HP1 KO MEFs.

(G) Quantification of IF mean intensities of H4K20me3 and H3K27me3 for shRNA of CTCF in NIH 3T3 cells. ***p < 0.0001.

and S5A). Further supporting the antagonism between HP1α and HP1β in PCH, CTCF EGFP was significantly scarcer in the PCH foci of HP1α-deficient MEFs, suggesting that HP1α is directly related to CTCF localization to PCH (Figure 4F). By contrast, a loss of HP1β induced, in around 45% of cells analyzed, a dramatic enrichment of CTCF in PCH regions (Figure 4F), which was correlated with a global increase in CTCF protein levels without altering CTCF gene expression (Figure S5D; data not shown). These data suggest that HP1β loss results in enhanced spreading of CTCF beyond its normal sites of localization. Confirming this hypothesis, CTCF was detected outside the H19 imprinting control region (H19-ICR) binding site in *Hp1β*$^{-/-}$ cells between 1 and 2 kb downstream of H19-ICR binding site 1 (ICR1) (Figure 4C). A similar observation was also observed at LINE-L1s elements (promoter and open reading frame [ORF]2), where a dramatic increase in CTCF levels was observed in *Hp1β*$^{-/-}$ cells. Together, these evidences indicate that HP1α and HP1β play opposite roles in CTCF distribution. For completeness, we explored the role of CTCF in regulating covalent histone modifications in PCH. As in the case of HP1α, shRNA-mediated depletion of CTCF induced a significant enrichment of H3K27me3 (2.6-fold) in PCH foci without any change in H4K20me3 levels

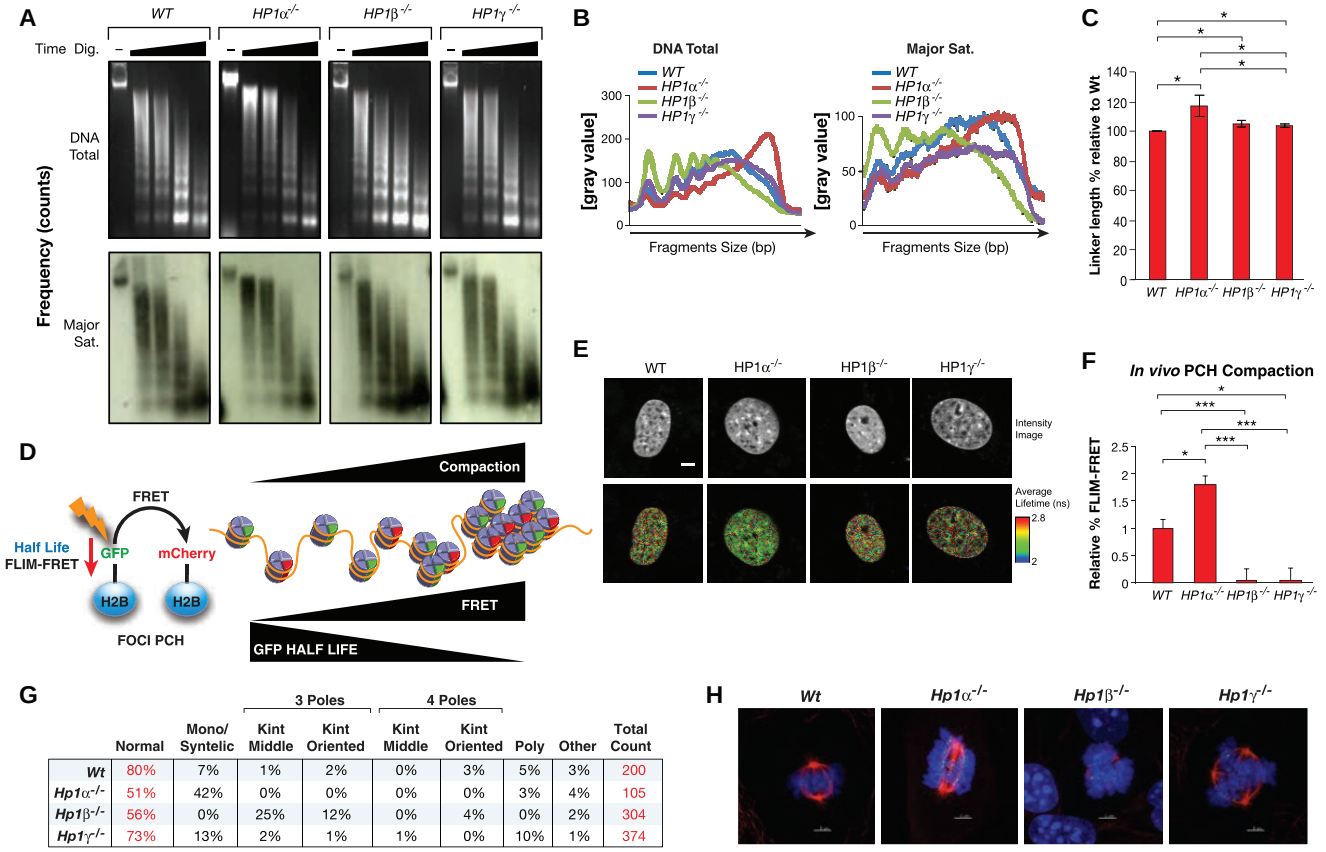

G

	Normal	Mono/ Syntelic	3 Poles Kint Middle	3 Poles Kint Oriented	4 Poles Kint Middle	4 Poles Kint Oriented	Poly	Other	Total Count
Wt	80%	7%	1%	2%	0%	3%	5%	3%	200
Hp1α-/-	51%	42%	0%	0%	0%	0%	3%	4%	105
Hp1β-/-	56%	0%	25%	12%	0%	4%	0%	2%	304
Hp1γ-/-	73%	13%	2%	1%	1%	0%	10%	1%	374

Figure 5. *In Vitro* and *In Vivo* Analysis of Chromatin Compaction in WT and HP1 KO Cells

(A) Upper panels: representative image of MNase digestion upon time for indicated MEFs. Lower panels: representative experiment of the corresponding southern blot incubated with a [^{32}P]-labeled major satellites probe.

(B) Quantification and intensity versus fragment-size representation of MNase digestion and southern blot line 3 from different experiments (n = 5).

(C) Linker-DNA length calculated from the experiment in (A) and represented in % compared to WT (see Experimental Procedures). *p < 0.05.

(D) Schematic representation of FLIM-FRET methodology used for *in vivo* chromatin compaction analysis based on H2B-GFP and H2B-mCherry co-expression (Llères et al., 2009). Lower GFP half-life means increased FRET levels and increased chromatin compaction.

(E) Representative images of FLIM-FRET experiments in the indicated MEFs. GFP intensity and GFP fluorophore lifetime-average images are shown.

(F) Relative quantification of chromatin compaction (%FRET) in indicated MEFs using FLIM-FRET methodology (Figures S5E and S5F). Absolute %FRET from Figure S5E relative to WT values is shown. Controls of these experiments are shown in Figure S5F. *p < 0.05,***p < 0.001.

(G) Analysis of mitotic defects in HP1 KO MEFs.

(H) Representative IF images of the defects included in (H). DAPI (blue), centromere marker, CREST (green), and tubulin (red) are shown.

or HP1α localization (Figures 4G and S5C). Altogether, these evidences suggest that CTCF collaborates with HP1α defining specific chromatin domains within PCH.

Depletion of HP1α, but Not of HP1β or HP1γ, Induces Decreased Accessibility and *In Vivo* Hypercompaction of PCH

A key question concerns the role of HP1 proteins in chromatin compaction. Such a role is implied by the observation that H4K20me3 has been directly linked to compaction levels in PCH foci through cohesins and that HP1 proteins recruit Suv420h2, which is the enzyme that is responsible for the trimethylation of H4K20 (Hahn et al., 2013). Accordingly, we investigated whether the changes that were observed in the HP1α- and HP1β-deficient cells were associated to changes in the levels of compaction of the PCH foci *in vitro* and *in vivo*. *In vitro*, we performed a classic micrococcal nuclease (MNase) digestion of the genome followed by a Southern blot with an [^{32}P]-labeled probe of the satellite. The loss of HP1α induced a decrease in accessibility of the PCH foci. By contrast, the loss of HP1β and, to a lesser extent, of HP1γ, induced enhanced digestion of PCH chromatin DNA by MNase (Figures 5A and 5B). This effect was not restricted to PCH foci but also affected the accessibility of chromatin globally. The loss of HP1α also resulted in around a 20% increase in linker-DNA length compared to WT cells (Figure 5C). Longer linker DNA has been associated with higher chromatin compaction (Szerlong and Hansen, 2011). Next, we investigated the effects of HP1 loss on chromatin compaction within PCH foci *in vivo* using FLIM-FRET assays. This method allowed us to measure the degree of compaction of both PCH foci and the whole genome in live cells by expressing H2B fused to two different fluorophores

(GFP and RFP) (Llères et al., 2009). Higher chromatin compaction was correlated with higher FRET efficiency between H2B-GFP and H2B-RFP, which resulted in a lower half-life of the FRET donor GFP (FLIM) (Figure 5D). A FLIM-FRET analysis of live cells confirmed results that were obtained *in vitro* because HP1α deficiency produced a decrease in the GFP half-life (πamp) as a consequence of a 1.8-fold increase in FRET efficiency. In contrast, HP1β- and HP1γ-deficient cells showed no significant changes in their GFP half-life (Figures 5E, 5F, S5E, and S5F). These results indicate that HP1α is a key player in the global organization of PCH by regulating its state of compaction.

Our *in vitro* and *in vivo* studies indicate that, in addition to a common redundant role of all three isoforms, HP1α and HP1β have unique isoform-specific roles in genome stability. To test this hypothesis, we studied the frequency of mitotic abnormalities in WT, *Hp1*$\alpha^{-/-}$, *Hp1*$\beta^{-/-}$, and *Hp1*$\gamma^{-/-}$ MEFs. Our results showed that *Hp1*$\alpha^{-/-}$ and *Hp1*$\beta^{-/-}$ harbored a higher frequency of aberrations compared to *Hp1*$\gamma^{-/-}$ or *Wt* cells. The *Hp1*$\alpha^{-/-}$ aberrations were strikingly different to those found in *Hp1*$\beta^{-/-}$ MEFs. The loss of HP1α resulted in an increased number of merotelic and syntelic attachment defects (Figure 5G), whereas the loss of HP1β resulted in high frequency of multipolar spindle formation. Interestingly, the loss of HP1γ resulted in less frequent defects that were a mixture of those found in *Hp1*$\alpha^{-/-}$ and *Hp1*$\beta^{-/-}$ MEFs, indicating that HP1γ shares some redundancy with the other isoforms (Figures 5G and 5H).

DISCUSSION

Our work suggests that each HP1 isoform makes a distinctive contribution to the organization and structure of PCH foci. The individual roles are most clearly manifest in chromosomal abnormalities found in isoform-specific mutant MEFs. The increased frequency of merotelic attachments found in *Hp1*$\alpha^{-/-}$, which resulted from the simultaneous binding of a single kinetochrore to both spindle poles (Figures 5G and 5H), have been previously associated to a deficient Clr4/Swi6 function in *Schizosaccharomyces pombe* (Gregan et al., 2007). By contrast, *Hp1*$\beta^{-/-}$ MEFs showed defects in mitotic spindle multipolarity (Figures 5G and 5H), which may be related to the de-condensed phenotype observed in these chromosomes. Our work indicates that HP1α plays a direct role in restraining H4K20me3 and H3K27me3 in PCH. Accordingly, we suggest that HP1α acts as an organizer of PCH in conjunction with CTCF. This is in agreement with the described localization of CTCF in centromeric/PCH regions (Mukhopadhyay et al., 2004; Rubio et al., 2008). Our data also suggest that HP1α may recruit CTCF to specific sites within PCH because the loss of HP1α causes a significant delocalization of CTCF-EGFP. Notably, we did not detect CTCF by ChIP in *WT*, *Hp1*$\alpha^{-/-}$, and *Hp1*$\gamma^{-/-}$ cells (Figure 4B) although the co-localization experiments of endogenous CTCF (Figure S5B) and GFP-CTCF distribution and FRET analysis (Figures 4E and 4F) confirmed the presence of CTCF in PCH as shown previously (Mukhopadhyay et al., 2004; Xiao et al., 2015). Our data suggest that HP1β act in opposition to HP1α with regard to H4K20me3 and H3K27me3 within PCH foci. Moreover, in *Hp1*$\beta^{-/-}$ cells, we observed a global enrichment of CTCF in large regions of the genome including PCH (Figure 4F), thereby suggesting a role for HP1β in restraining the localization of CTCF to specific loci and, thereby, likely controlling chromatin boundaries. This role is supported by our observation that loss of HP1β results in enrichment of CTCF outside its normal confines. Specifically, we observed that, in *Hp1*$\beta^{-/-}$ cells, CTCF is found in the 6-kb-long LINE-L1 elements at the promoter and also 2 kb away, at the ORF2 (Figure 4C). A similar observation was observed at the H19 ICR in *Hp1*$\beta^{-/-}$ cells (Figure 4C). The latter result is in keeping with the suggestion that HP1β may regulate genomic imprinting (Singh, 2016). Because there does not appear to be any CTCF canonical motifs downstream of the H19 ICR or in LINE-L1s, the observed spreading is unlikely to be related to a direct binding of CTCF to DNA but more likely dependent on other factors.

Our work suggests that the relationship between H3K27me3 and H4K20me3 with HP1α is different. The increased levels of H3K27me3, but not of H4K20me3, that were observed upon downregulation of HP1α suggest that the specific regulation of H4K20me3 may be restricted to an earlier developmental stage prior to the specification of the fibroblast lineage. In support of this idea, the establishment of both HP1α and H4K20me3 seems to take place at the same time during late development (Wongtawan et al., 2011). Recent work has suggested that HP1α has a more significant role in the establishment of H3K9me3 mark than in its maintenance (Hathaway et al., 2012). This function may also be true for H4K20me3 since the re-expression of HP1α in *Hp1*$\alpha^{-/-}$ could re-establish the H4K20me3 levels in PCH, but its re-deletion did not have any clear effect (Figures 2A–2C).

We have also revealed an unexpected link between HP1β and H4K20me3. *In vivo* HP1β preferentially interacts with Suv420h2 within the PCH foci and regulates its dynamics. Consistently, HP1β recognizes H4K20me3-methylated peptides and HP1β-containing chromatin is enriched in H4K20me3 and tends to localize with H4K20me3 in major satellites compared to other isoforms. Moreover, a ChIP-seq analysis shows a higher genome-wide correlation in ESCs between HP1β and H4K20me3 compared to HP1α.

One of the most striking observations that we found was the hypercompaction of the PCH structure in HP1α-deficient cells. Hypercompaction in HP1α-deficient cells was associated with an increased enrichment in H4K20me3 and H3K27me3 and a longer linker DNA (Figure 5C). This result was surprising because a previous study reported that artificial binding of LacR-tagged HP1α or HP1β to Lac operon-regulated transgenes resulted in chromatin compaction (Verschure et al., 2005). These apparently conflicting observations may be reconciled if one population of HP1α molecules is involved in PCH compartmentalization while another plays, along with the other isoforms, a more redundant role.

Based on our data, we propose that, despite a well-established functional redundancy between isoforms in PCH, HP1α and HP1β play different roles in the organization and structure of PCH. Our studies also suggest a model of heterochromatin organization whereby HP1α maintains, together with CTCF, the internal structure and compaction of PCH foci by restricting the distribution of H4K20me3 and H3K27me3. These findings offer

insight into the structural organization of the genome and provide a perspective on the role of HP1 isoforms and their functional link with heterochromatin structure, genome organization, and stability.

EXPERIMENTAL PROCEDURES

FRET, FLIM-FRET, and FRAP Assays

Leica SP5 confocal and Acceptor photo-bleaching methods were used to measure the FRET in PCH foci. %FRET was calculated taking 100% as the FRET value that was obtained for GFP-RPF (positive control) and 0% as the value obtained for the FRET value that was obtained for the donor construct alone. RFP protein from PCH foci was bleached by using a maximum laser 561 power obtaining ~80% of acceptor-intensity bleaching. The FLIM-FRET experiments were performed as indicated (see Supplemental Experimental Procedures). All experiments were performed at least in 10 independent assays and on 50 different cells. FRAP experiments were carried out as previously described (see Supplemental Experimental Procedures).

Generation of noKO and reKO Cells

The generation of *Hp1α*$^{-/-}$, *Hp1β*$^{-/-}$, and *Hp1γ*$^{-/-}$ mouse and associated MEFs was previously described (Aucott et al., 2008; Brown et al., 2010; Maksakova et al., 2011). The process of conversion from KO to reKO was similar as it was shown for *Hp1γ*$^{-/-}$(Brown et al., 2010). *Hp1α*$^{-/-}$ (*Cbx5*$^{-/-}$) (KO) MEFs were converted into noKO (WT) by the overexpression of Cre recombinase (R1) in the *Hp1α*$^{-/-}$ MEF cells resulting in the release of the Neo cassette and the restoration of HP1α gene integrity and expression (noKO). Subsequently, the generation of reKO cells was performed by overexpression of FLP recombinase (R2) in noKO cells, which resulted in a partial deletion of the *Hp1α*$^{-/-}$ gene and complete abrogation of HP1 expression.

ChIPs and re-ChIPs

ChIPs were performed with 3–5 × 10^6 cells as previously described (Rodríguez-Ubreva and Ballestar, 2014). In re-ChIP experiments, the first ChIP (HP1) was eluted with 10 mM Tris-EDTA (TE) and 20 mM DTT and diluted 20 times in dilution buffer (0.01% SDS, 1.1% Triton X-100, 1.2 mM EDTA, 16.7 mM Tris-HCl 8.1, 167 mM NaCl, and protease inhibitors) and proceeded to the second ChIP (H3K20me3 or H3K9me3).

Peptide Pull-Down of HP1 Isoforms

Biotinylated peptides spanning histone H4 residues 1–23 or 1–21 of H3 (unmodified or H3K9me3) were obtained from Anaspec (Fremont, CA). 100 μg of peptides were pre-bound to streptavidin agarose (Millipore) and then incubated at 4°C overnight (O/N) with nuclear extracts from 293F cells expressing the HA-tagged HP1 isoforms either prepared according to the Dignam or RIPA method (see Supplemental Experimental Procedures).

Statistical Analysis

The statistical analysis was performed using a multivariant ANOVA (immunofluorescence [IF] analysis, ChIP-seq, FLIM-FRET) or Student's t test (rest of analysis). Graph values represent mean values of $n \geq 3$ experiments and include SEs except in the case of ChIP-seq (SDs). The specific n of each quantification and p values are indicated in the corresponding figure legends.

SUPPLEMENTAL INFORMATION

Supplemental Information includes Supplemental Experimental Procedures and five figures and can be found with this article online at https://doi.org/10.1016/j.celrep.2017.10.092.

AUTHOR CONTRIBUTIONS

A.V. and L.B.-P. conceived the study and designed the experiments. A.V. supervised the work. A.V. and P.B.S. wrote the manuscript. L.B.-P. performed the experiments. H.R.-V. and J.G. supported the performance of the experiments; L.S., P.B.S., G.S., and J.A. collaborated in the discussion. L.S., J.K.T., and N.K.-G. performed FRAP and IF quantifications. P.B.S. and J.P.B. generated the MEF KO cells. G.S. generated the Suv420h2-EGFP vector. C.C., L.B.-P., and T.Z. carried out the FLIM-FRET experiment. M.V. and M.E. carried out methylation assays. A.G. performed the ChIP-seq bioinformatic analysis.

ACKNOWLEDGMENTS

We thank the members of the Vaquero laboratory, Dr. Karen Schindler, Dr. Sònia Guil, and Dr. Javier Rodriguez-Ubreva, for support and fruitful discussion; Raquel García and the CRG Microscopy Unit for support on FLIM-FRET experiments; and David Llères, Angus I. Lamond, Victor V. Lobanenkov, Mien-Chie Hung, Alan Underhill, Peter Hemmerich, Chris Wilson, and Masayuki Sekimata for sharing reagents. This work was supported by the Spanish Ministry of Economy and Competitiveness (MINECO) (SAF2011-25860 and SAF2014-55964R to A.V.) and cofunded by FEDER funds/European Regional Development Fund (ERDF)—a way to build Europe, the Catalan Government Agency AGAUR (2009SGR-914 and 2014SGR-400 to A.V.), HGINJ (to L.S.), Deutsche Forschungsgemeinschaft (SFB1064 to G.S.), and the Canadian Institutes of Health Research (CIHR) (MOP-97878 to J.A.).

Received: February 13, 2017
Revised: September 15, 2017
Accepted: October 24, 2017
Published: November 21, 2017

REFERENCES

Agirre, E., Bellora, N., Alló, M., Pagès, A., Bertucci, P., Kornblihtt, A.R., and Eyras, E. (2015). A chromatin code for alternative splicing involving a putative association between CTCF and HP1α proteins. BMC Biol. *13*, 31.

Aucott, R., Bullwinkel, J., Yu, Y., Shi, W., Billur, M., Brown, J.P., Menzel, U., Kioussis, D., Wang, G., Reisert, I., et al. (2008). HP1-beta is required for development of the cerebral neocortex and neuromuscular junctions. J. Cell Biol. *183*, 597–606.

Bannister, A.J., Zegerman, P., Partridge, J.F., Miska, E.A., Thomas, J.O., Allshire, R.C., and Kouzarides, T. (2001). Selective recognition of methylated lysine 9 on histone H3 by the HP1 chromo domain. Nature *410*, 120–124.

Benayoun, B.A., Pollina, E.A., and Brunet, A. (2015). Epigenetic regulation of ageing: linking environmental inputs to genomic stability. Nat. Rev. Mol. Cell Biol. *16*, 593–610.

Brown, J.P., Bullwinkel, J., Baron-Lühr, B., Billur, M., Schneider, P., Winking, H., and Singh, P.B. (2010). HP1gamma function is required for male germ cell survival and spermatogenesis. Epigenetics Chromatin *3*, 9.

Canzio, D., Larson, A., and Narlikar, G.J. (2014). Mechanisms of functional promiscuity by HP1 proteins. Trends Cell Biol. *24*, 377–386.

Carone, D.M., and Lawrence, J.B. (2013). Heterochromatin instability in cancer: from the Barr body to satellites and the nuclear periphery. Semin. Cancer Biol. *23*, 99–108.

Cuddapah, S., Jothi, R., Schones, D.E., Roh, T.Y., Cui, K., and Zhao, K. (2009). Global analysis of the insulator binding protein CTCF in chromatin barrier regions reveals demarcation of active and repressive domains. Genome Res. *19*, 24–32.

Dialynas, G.K., Terjung, S., Brown, J.P., Aucott, R.L., Baron-Luhr, B., Singh, P.B., and Georgatos, S.D. (2007). Plasticity of HP1 proteins in mammalian cells. J. Cell Sci. *120*, 3415–3424.

Eissenberg, J.C., James, T.C., Foster-Hartnett, D.M., Hartnett, T., Ngan, V., and Elgin, S.C. (1990). Mutation in a heterochromatin-specific chromosomal protein is associated with suppression of position-effect variegation in Drosophila melanogaster. Proc. Natl. Acad. Sci. USA *87*, 9923–9927.

Fuks, F., Hurd, P.J., Deplus, R., and Kouzarides, T. (2003). The DNA methyltransferases associate with HP1 and the SUV39H1 histone methyltransferase. Nucleic Acids Res. *31*, 2305–2312.

Gregan, J., Riedel, C.G., Pidoux, A.L., Katou, Y., Rumpf, C., Schleiffer, A., Kearsey, S.E., Shirahige, K., Allshire, R.C., and Nasmyth, K. (2007). The kinetochore proteins Pcs1 and Mde4 and heterochromatin are required to prevent merotelic orientation. Curr. Biol. *17*, 1190–1200.

Hahn, M., Dambacher, S., Dulev, S., Kuznetsova, A.Y., Eck, S., Wörz, S., Sadic, D., Schulte, M., Mallm, J.P., Maiser, A., et al. (2013). Suv4-20h2 mediates chromatin compaction and is important for cohesin recruitment to heterochromatin. Genes Dev. *27*, 859–872.

Hathaway, N.A., Bell, O., Hodges, C., Miller, E.L., Neel, D.S., and Crabtree, G.R. (2012). Dynamics and memory of heterochromatin in living cells. Cell *149*, 1447–1460.

Hiragami-Hamada, K., Soeroes, S., Nikolov, M., Wilkins, B., Kreuz, S., Chen, C., De La Rosa-Velázquez, I.A., Zenn, H.M., Kost, N., Pohl, W., et al. (2016). Dynamic and flexible H3K9me3 bridging via HP1β dimerization establishes a plastic state of condensed chromatin. Nat. Commun. *7*, 11310.

Jones, D.O., Cowell, I.G., and Singh, P.B. (2000). Mammalian chromodomain proteins: their role in genome organisation and expression. BioEssays *22*, 124–137.

Kwon, S.H., and Workman, J.L. (2011). The changing faces of HP1: From heterochromatin formation and gene silencing to euchromatic gene expression: HP1 acts as a positive regulator of transcription. BioEssays *33*, 280–289.

Lachner, M., O'Carroll, D., Rea, S., Mechtler, K., and Jenuwein, T. (2001). Methylation of histone H3 lysine 9 creates a binding site for HP1 proteins. Nature *410*, 116–120.

Larson, A.G., Elnatan, D., Keenen, M.M., Trnka, M.J., Johnston, J.B., Burlingame, A.L., Agard, D.A., Redding, S., and Narlikar, G.J. (2017). Liquid droplet formation by HP1α suggests a role for phase separation in heterochromatin. Nature *547*, 236–240.

Llères, D., James, J., Swift, S., Norman, D.G., and Lamond, A.I. (2009). Quantitative analysis of chromatin compaction in living cells using FLIM-FRET. J. Cell Biol. *187*, 481–496.

Maison, C., and Almouzni, G. (2004). HP1 and the dynamics of heterochromatin maintenance. Nat. Rev. Mol. Cell Biol. *5*, 296–304.

Maksakova, I.A., Goyal, P., Bullwinkel, J., Brown, J.P., Bilenky, M., Mager, D.L., Singh, P.B., and Lorincz, M.C. (2011). H3K9me3-binding proteins are dispensable for SETDB1/H3K9me3-dependent retroviral silencing. Epigenetics Chromatin *4*, 12.

Mukhopadhyay, R., Yu, W., Whitehead, J., Xu, J., Lezcano, M., Pack, S., Kanduri, C., Kanduri, M., Ginjala, V., Vostrov, A., et al. (2004). The binding sites for the chromatin insulator protein CTCF map to DNA methylation-free domains genome-wide. Genome Res. *14*, 1594–1602.

Raurell-Vila, H., Bosch-Presegue, L., Gonzalez, J., Kane-Goldsmith, N., Casal, C., Brown, J.P., Marazuela-Duque, A., Singh, P.B., Serrano, L., and Vaquero, A. (2017). An HP1 isoform-specific feedback mechanism regulates Suv39h1 activity under stress conditions. Epigenetics *12*, 166–175.

Rea, S., Eisenhaber, F., O'Carroll, D., Strahl, B.D., Sun, Z.W., Schmid, M., Opravil, S., Mechtler, K., Ponting, C.P., Allis, C.D., and Jenuwein, T. (2000). Regulation of chromatin structure by site-specific histone H3 methyltransferases. Nature *406*, 593–599.

Rodríguez-Ubreva, J., and Ballestar, E. (2014). Chromatin immunoprecipitation. Methods Mol. Biol. *1094*, 309–318.

Rubio, E.D., Reiss, D.J., Welcsh, P.L., Disteche, C.M., Filippova, G.N., Baliga, N.S., Aebersold, R., Ranish, J.A., and Krumm, A. (2008). CTCF physically links cohesin to chromatin. Proc. Natl. Acad. Sci. USA *105*, 8309–8314.

Saksouk, N., Simboeck, E., and Déjardin, J. (2015). Constitutive heterochromatin formation and transcription in mammals. Epigenetics Chromatin *8*, 3.

Schotta, G., Lachner, M., Sarma, K., Ebert, A., Sengupta, R., Reuter, G., Reinberg, D., and Jenuwein, T. (2004). A silencing pathway to induce H3-K9 and H4-K20 trimethylation at constitutive heterochromatin. Genes Dev. *18*, 1251–1262.

Singh, P.B. (2010). HP1 proteins–what is the essential interaction? Genetika *46*, 1424–1429.

Singh, P.B. (2016). Heterochromatin and the molecular mechanisms of 'parent-of-origin' effects in animals. J. Biosci. *41*, 759–786.

Strom, A.R., Emelyanov, A.V., Mir, M., Fyodorov, D.V., Darzacq, X., and Karpen, G.H. (2017). Phase separation drives heterochromatin domain formation. Nature *547*, 241–245.

Szerlong, H.J., and Hansen, J.C. (2011). Nucleosome distribution and linker DNA: connecting nuclear function to dynamic chromatin structure. Biochem. Cell Biol. *89*, 24–34.

Verschure, P.J., van der Kraan, I., de Leeuw, W., van der Vlag, J., Carpenter, A.E., Belmont, A.S., and van Driel, R. (2005). In vivo HP1 targeting causes large-scale chromatin condensation and enhanced histone lysine methylation. Mol. Cell. Biol. *25*, 4552–4564.

Wongtawan, T., Taylor, J.E., Lawson, K.A., Wilmut, I., and Pennings, S. (2011). Histone H4K20me3 and HP1α are late heterochromatin markers in development, but present in undifferentiated embryonic stem cells. J. Cell Sci. *124*, 1878–1890.

Xiao, T., Wongtrakoongate, P., Trainor, C., and Felsenfeld, G. (2015). CTCF recruits centromeric protein CENP-E to the pericentromeric/centromeric regions of chromosomes through unusual CTCF-binding sites. Cell Rep. *12*, 1704–1714.

Cell Reports, Volume *21*

Supplemental Information

Mammalian HP1 Isoforms Have Specific Roles in Heterochromatin Structure and Organization

Laia Bosch-Presegué, Helena Raurell-Vila, Joshua K. Thackray, Jessica González, Carmen Casal, Noriko Kane-Goldsmith, Miguel Vizoso, Jeremy P. Brown, Antonio Gómez, Juan Ausió, Timo Zimmermann, Manel Esteller, Gunnar Schotta, Prim B. Singh, Lourdes Serrano, and Alejandro Vaquero

A

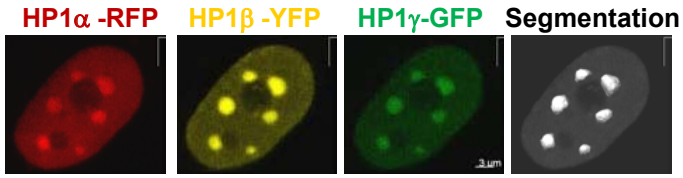

B

Pair	Coefficient
HP1α-RFP_vs_HP1β-YFP	0.4679
HP1α-RFP_vs_HP1γ-GFP	0.28125
HP1β-YFP_vs_HP1γ-GFP	0.24951
HP1α-RFP_vs_Radial Position	-0.54321
HP1βYFP_vs_Radial Position	-0.54219
HP1γ-GFP_vs_Radial Position	-0.20241

C

Correlation	Slope	Intercept	r	P-value	StdErr
HP1α-RFP_vs_HP1β-YFP	0.428	0.2273	0.4477	0.00E+00	0.0016
HP1α-RFP_vs_HP1γ-GFP	0.2815	0.1927	0.2825	0.00E+00	0.0017
HP1β-YFP_vs_HP1γ-GFP	0.2493	0.2224	0.2392	0.00E+00	0.0018
HP1α-RFP_vs_Radial Position	-0.40458	0.79956	-0.54084	0.00E+00	1.15E-03
HP1β-YFP_vs_Radial Position	-0.38162	0.72704	-0.53363	0.00E+00	1.10E-03
HP1γ-GFP_vs_Radial Position	-0.15027	0.44529	-0.20162	0.00E+00	1.33E-03

D

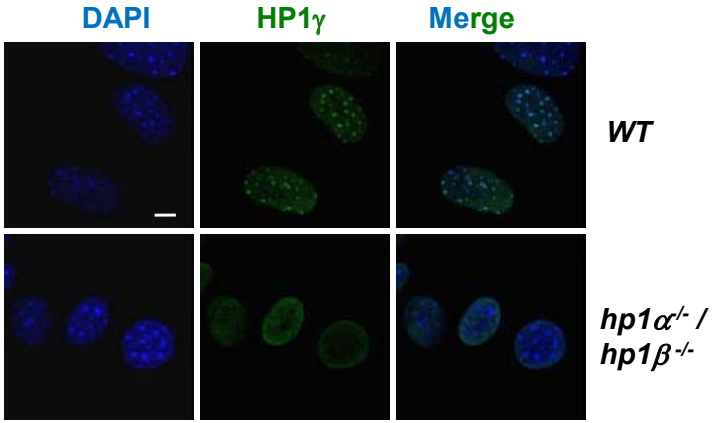

E

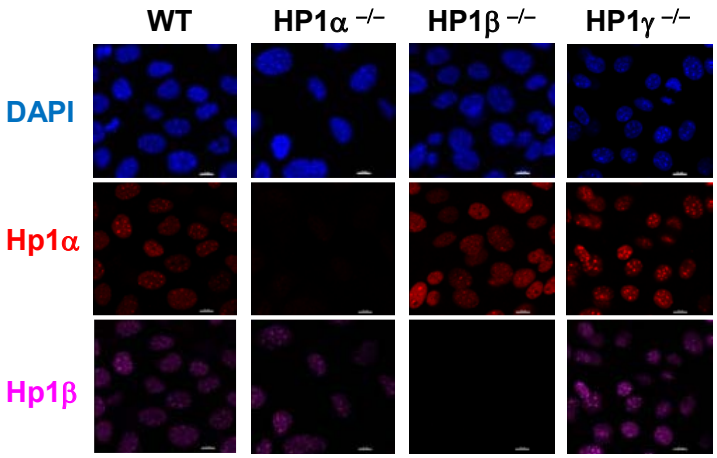

F

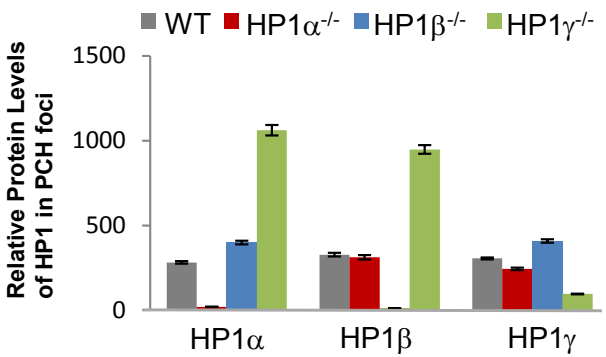

Figure S1. Related to Figure 1. HP1 α, β and γ distribution in the PCH foci. (A) Representative fluorescence images of HP1α-RFP, HP1β-YFP and HP1γ-GFP PCH co-localization in NIH3T3 cells used in B-D analysis. The right image shows the segmentation of the PCH based on combined intensity of the three HP1 isoforms. **(B),(C).** Table showing the spearman rank-order correlation coefficients (B) and the linear least-squares regression (C) for the 2D-histogram analysis shown in Figure 1A. Slope is the slope of the regression line, intercept is the y-intercept of the regression line, r is the correlation coefficient of the regression, p-value is the two-sided p-value for a hypothesis test whose null hypothesis is that the slope is zero, and stderr is the standard error of the estimated slope. **(D)** Cell distribution of endogenous HP1γ in MEFs deficient for both HP1α and HP1β. **(E)** Immunofluorescence of endogenous HP1 isoforms in *WT, hp1α-/-* and *hp1β-/-* MEFs. **(F)** Quantification of n=3 experiments performed as in (E).

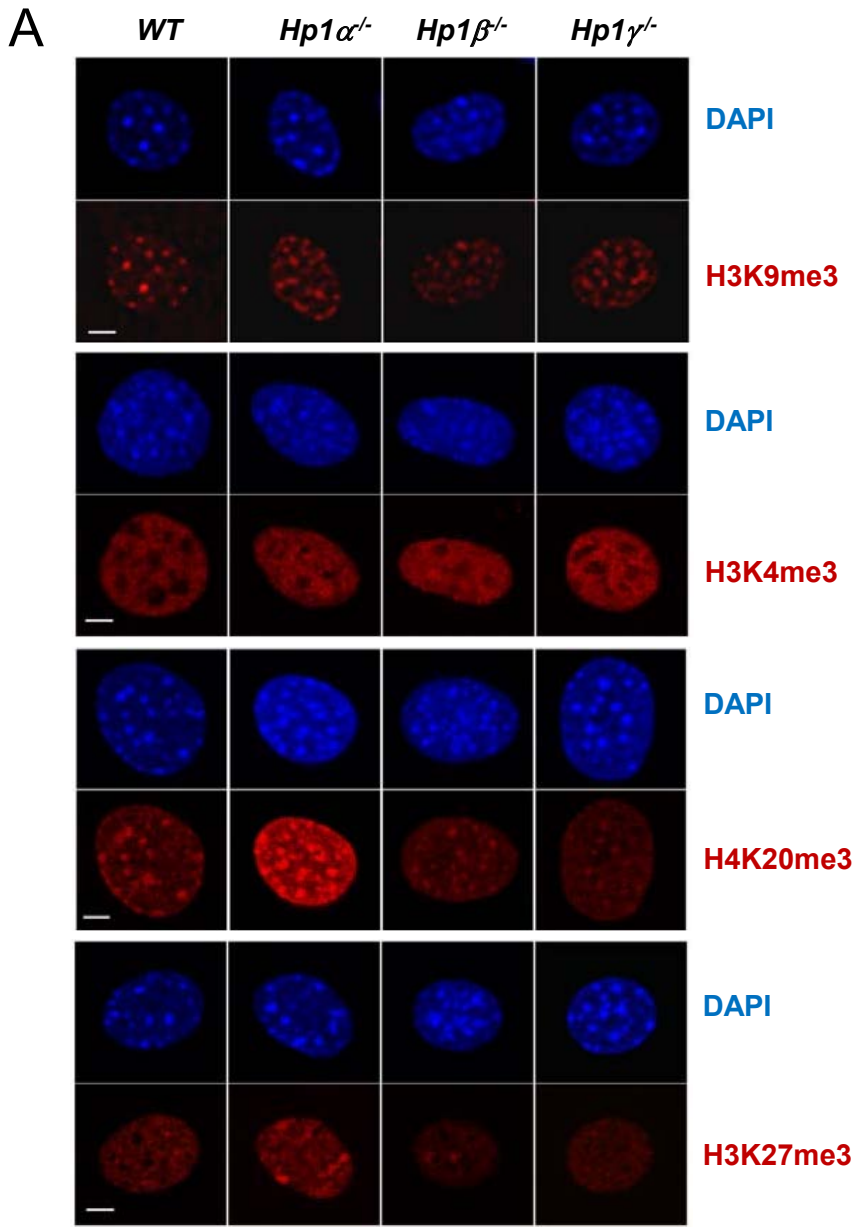

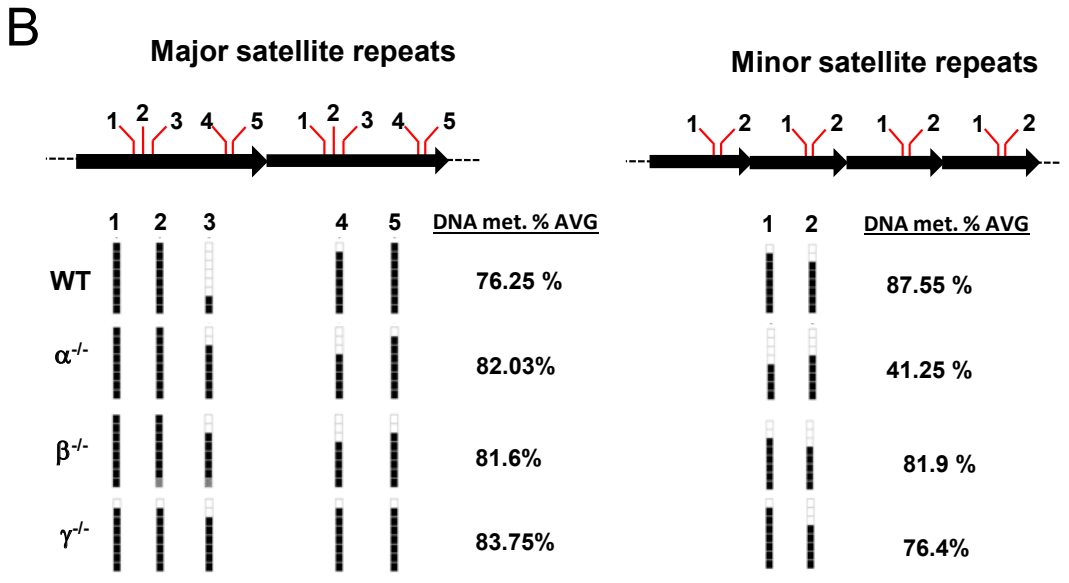

C

	Minor Satellites		Major Satellites				
Pos.	**1**	**2**	**1**	**2**	**3**	**4**	**5**
Wt* vs *HP1α-/-	0.102	0.0552	0.5	0.324	0.2266	0.449	0.136
Wt* vs *HP1β-/-	0.3492	0.3492	0.349	0.271	0.2712	0.385	3.12E-12
Wt* vs *HP1γ-/-	0.1464	0.1646	0.349	0.2712	0.2712	0.2958	1.25-11

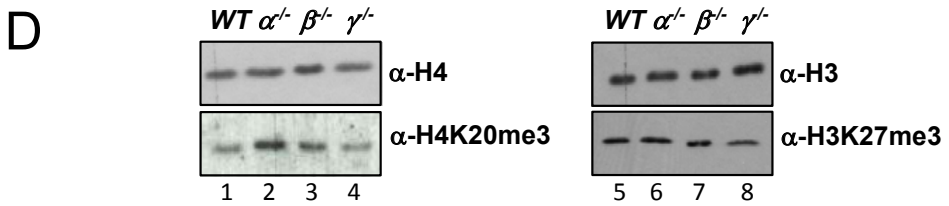

Figure S2. Related to Figure 1. (A) Representative immunofluorescence images of the experiments described in Figure 1B. Only PCH regions were included in the analysis (DAPI-strongly stained foci). **(B)** Representative bisulfite genomic sequencing in the major (upper panel) and minor (lower panel) satellite repeats of murine cells knockdown for the three mammalian HP1 isoforms. Bisulfite genomic sequencing of eight individual clones in the major and minor satellite CpG sites was used to determine DNA methylation status in the wild-type condition and after the depletion of the α, β, and . isoforms, respectively. Percentages represent the DNA methylation average from two to three independent replicates. Presence of a methylated or unmethylated cytosine is indicated by a black or a white square, respectively. **(C)** A T-student test was performed in the indicated results. The p value is shown in each case for each position of Minor and Major satellites. Only the difference in Major Satellite position 5 between WT vs HP1β$^{-/-}$ and WT vs HP1γ$^{-/-}$ was statistically significant. However, these differences were not considered biologically relevant as all three cell lines showed a % of methylation above 60% in this position. WT (80%),; HP1β$^{-/-}$ (60%); HP1γ$^{-/-}$ (70%). **(D)** H4K20me3 and H3K27me3 levels (WB) in these MEFs.

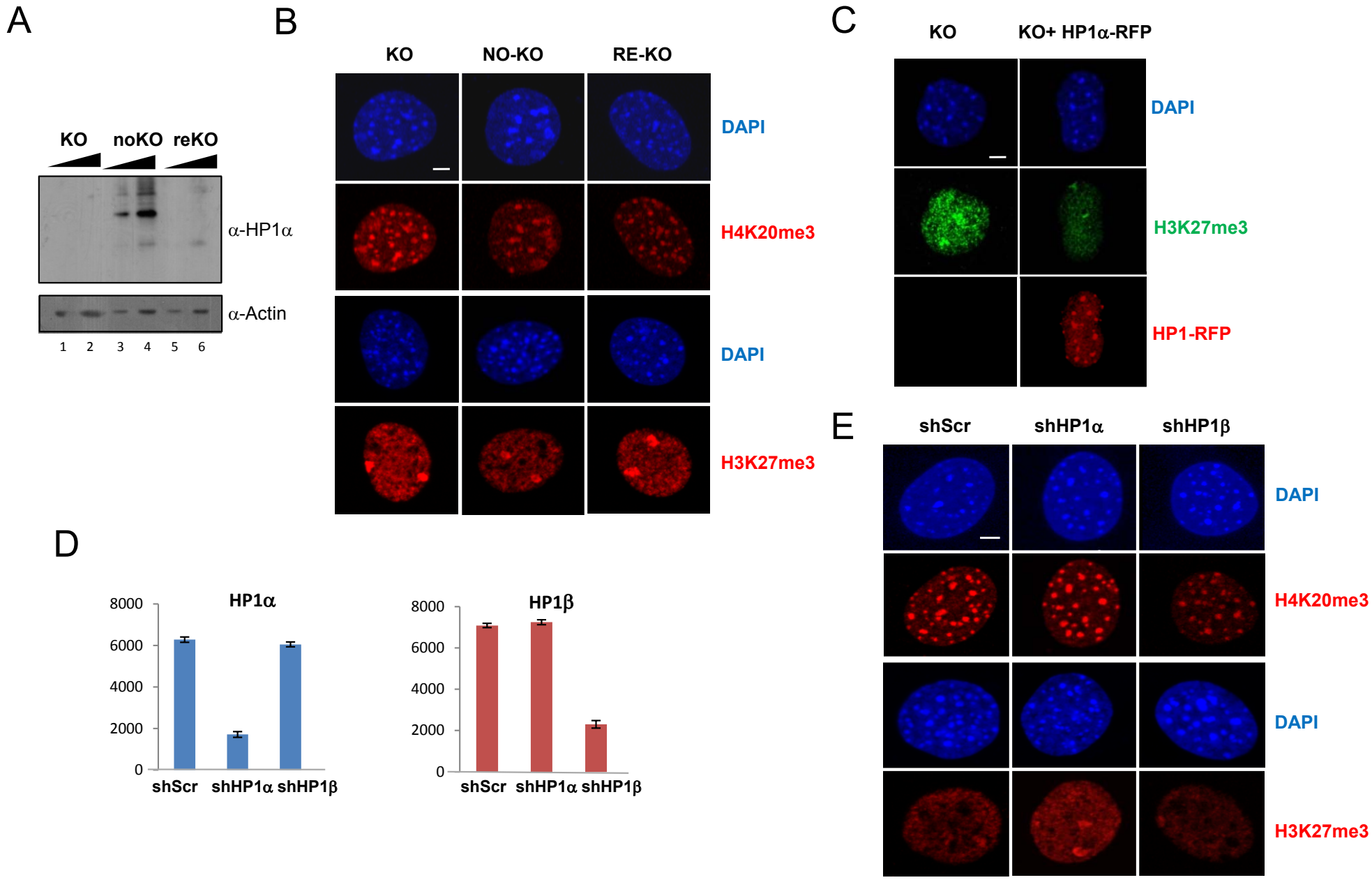

Figure S3. Related to Figure 2. (A) Western-blot of HP1α in KO, noKO and reKO cells described in Figure 2A. **(B)** Representative immunofluorescence images of the experiments described in Figure 2B. **(C)** Representative immunofluorescence images of the H3K27me3 experiments described in Figure 2C. **(D)** Efficiency of HP1α and HP1β shRNA mediated knockdown. Quantification of mean intensity of the corresponding HP1 isoforms measured by quantitative IF. **(E)** Representative immunofluorescence images of the experiments described in Figure 2D.

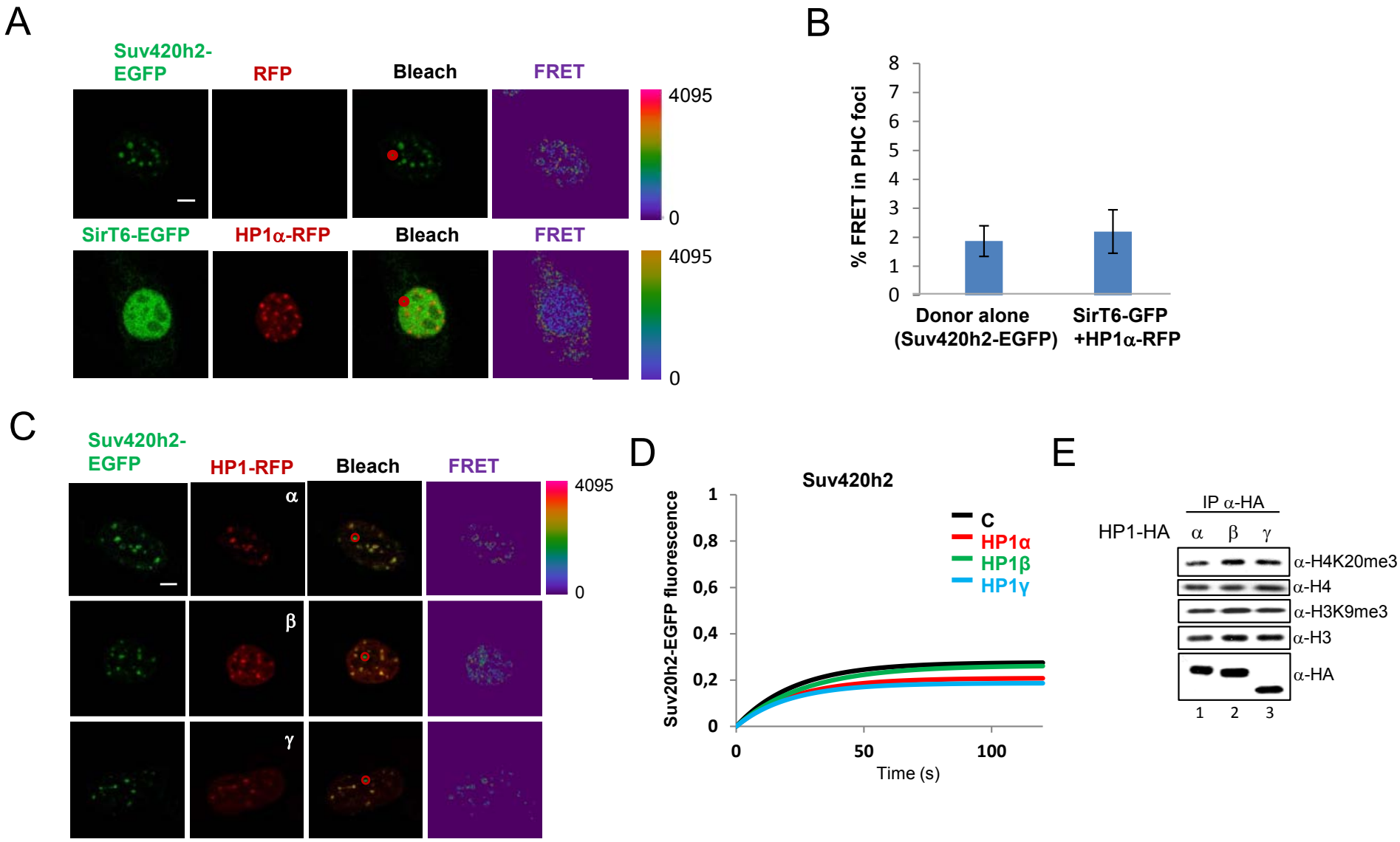

Figure S4. Related to Figure 3. (A)-(B) Negative controls of FRET experiments. **(A)** Representative images of FRET experiments either using Donor alone (in this case Suv420h2-EGFP) or a donor that binds to chromatin but does not interact with HP1α, SirT6-EGFP, and HP1α-RFP. **(B)** Quantification of n=3 FRET experiments as the ones in (A). **(C)** Representative images of the FRET experiments between Suv420h2-EGFP and the RFP-tagged HP1 isoforms. The red circle indicates the bleaching area. The quantification is shown in Fig 3B. **(D)** FRAP assay of Suv4-20h2 on PCH foci in NIH3T3 cells upon overexpression of empty vector (C), HP1α, β or γ. The quantification and statistical analysis of the FRAPs are shown in Figure 3D. **(E)** Representative pull-down assay of the quantification shown in Figure 3E.

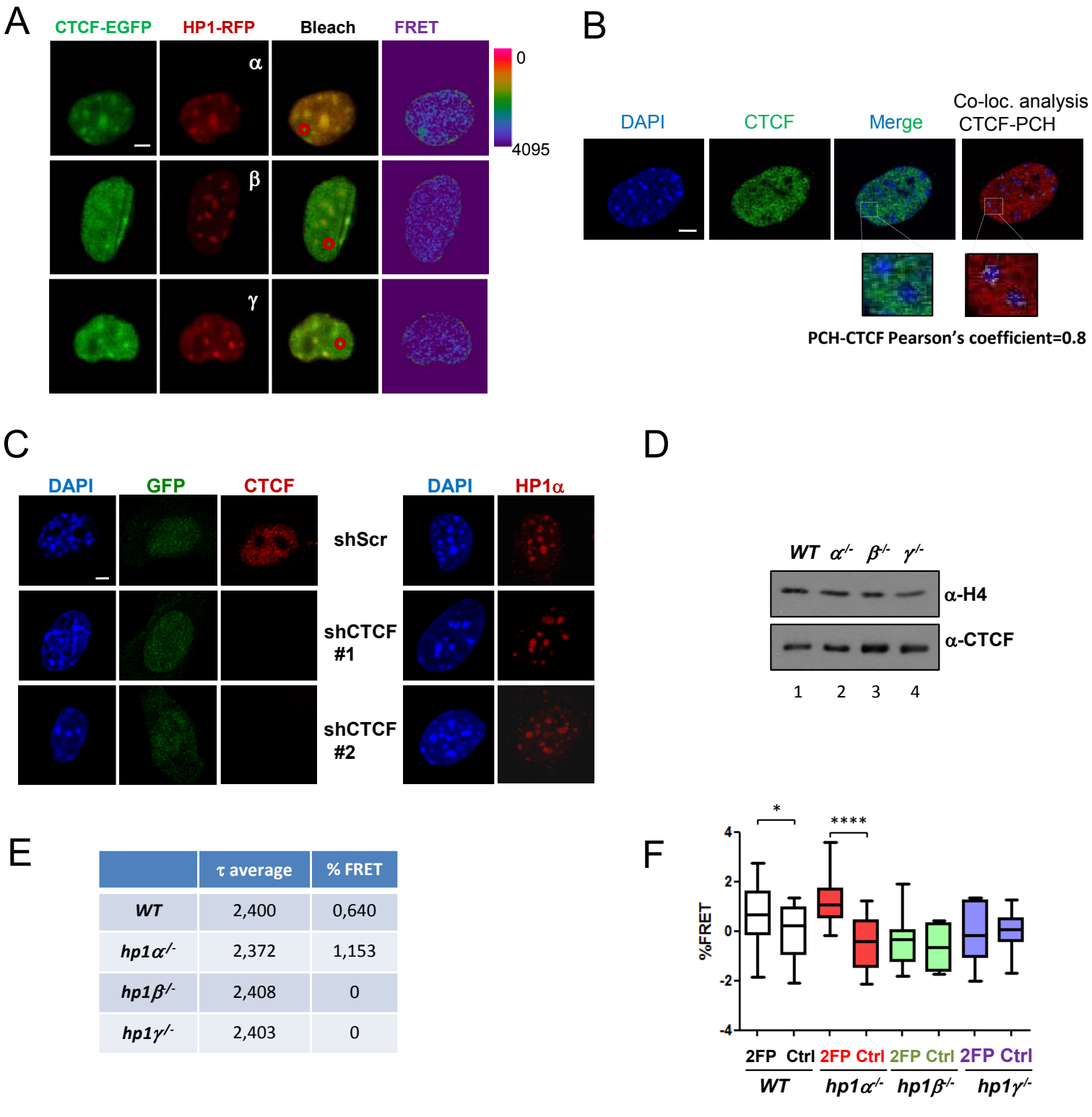

	τ average	% FRET
WT	2,400	0,640
hp1α$^{-/-}$	2,372	1,153
hp1β$^{-/-}$	2,408	0
hp1γ$^{-/-}$	2,403	0

Figure S5. Related to Figure 4 and 5. (A) Representative images of the FRET experiments between CTCF and the HP1 isoforms. The quantification is shown in Fig 4E. **(B)** Distribution of endogenous CTCF in PCH of WT MEFs. IF of DNA (DAPI), CTCF and Merge of both are shown. Right image, co-localization analysis of CTCF in DAPI-stained PCH foci signal. For clarification's sake, only PCH DAPI is shown. Positive co-localization of CTCF signal (red) with PCH foci are shown in white. Co-localization analysis resulted in a Pearson's correlation coefficient of 0.8 **(C)** Effect of two different CTCF shRNAs on CTCF (left) and HP1α (right) levels by immunofluorescence. **(D)** Representative western-blot of the levels of CTCF in the indicated MEFs. Histone H4 is also shown as a loading control. **(E)** Summary Table of FLIM-FRET experiment shown in Figure 5D-F. The quantification of τ average (relative half-life of H2B-GFP in the presence of H2B-RFP acceptor fluorophore), and %FRET (FRET efficiency of H2B-GFP and H2B-RFP (2FP) compared to the same cells expressing H2B-GFP alone (Ctrl)), are shown. **(F)** Control experiment to confirm that FRET % variations are not intrinsic variations/reductions of lifetime caused by environmental conditions, intraFRET events or quenching. For that purpose, GFP-H2B cells were analyzed by applying a tri-exponential model where we fixed two of the lifetime with the previous value from the τ average obtained in the no-FRET conditions. Statistical analysis of FRET efficiency of each cell population between each 2FP and its own control showed they were significantly different only in the case of *WT* and HP1α-deficient cells MEFs with a p-value<0.05 (*WT*) and 0.0001 (*hp1α*$^{-/-}$), respectively.

Supplementary Experimental Procedures

Plasmids and Antibodies

Expression vectors of FLAG or HA-tagged HP1 isoforms (FLAG-HP1α/β/γ and HP1-HAα/β/γ, respectively) were generated in pcDNA4T0 (Invitrogen) by standard PCR-based cloning strategy from HP1-GFP vectors generously provided by Dr Peter Hemmerich (Leibniz Institute for Age Research, Jena, Germany). Myc-Suv39h1, FLAG-Ezh2, H2AZ.1-GFP plasmids were previously described (Dryhurst et al., 2009; Kuzmichev et al., 2005; Vaquero et al., 2007). shRNA vectors of mouse HP1α and β were obtained from Dharmacon (GE-Healthcare). pCISuv4-20h2-HA, Myc-Ezh2, CTCF-GFP, H2B-GFP and H2B-mCherry constructs were generously provided by Dr Alan Underhill (Univ. Alberta, Canada)(Tsang et al., 2010), Dr. Mien-Chie Hung (MD Anderson Cancer Center Houston, USA)(Yu et al., 2013), and Dr Victor V.Lobanenkov (NIH, USA), Dr Angus I. Lamond (Univ. Dundee, UK) and Dr David Llères (IGMM, Molpellier, France)(Lleres et al., 2009), respectively. FLIM-FRET experiment vectors The CTCF shRNA vectors were a generous gift from Dr Chris Wilson (University of Washington, Seattle, USA) and Dr Masayuki Sekimata (Fukushima Univ, Japan) (Sekimata et al., 2009).

HP1α, β and γ specific antibodies were obtained from Euromedex (IF and WB) and Abcam (ChIP). Other primary antibodies used in this work were: α-H3K9me3, α-H4K20me3, α-Smc3, α-H2AZ and α-H4 (Abcam); α-H3K27me3 (IF), α-H3, α-CTCF, and α-Myc tag (Cell signaling); α-GFP, α-H3K27me3 (ChIP), α-CTCF and rabbit Igs (ChIP) (Millipore); α-FLAG M2, α-HA and α-Tubulin (Sigma-Aldrich); α-H3K4me3 (Active motif); CREST (Antibodies Incorporated). Regarding secondary antibodies, anti-rabbit and anti-mouse HRP-conjugated antibodies (Sigma-Aldrich) were used for western-blots, and Alexa Flour 488 and 561 and 647 for immunofluorescence experiments (Molecular Probes).

Immunofluorescence

Immunofluorescence experiments were performed as described elsewhere(Vaquero et al., 2007; Vaquero et al., 2006). Acquired image stacks were processed by Huygens deconvolution software (Scientific Volume Imaging). Three-dimensional reconstructions, computer-generated visualization of the signal and image analysis were obtained using Imaris software (Bitplane, A.G.). Cell cycle discrimination of exponentially growing cells was performed as previously described (Serrano et al., 2011). Cells were then fixed with paraformaldehyde and mounted with SlowFade Gold antifade pmedia (ThermoFisher). 3D spectral imaging was performed using a Zeiss LSM510 Meta confocal microscope equipped with a C. Apochromat 63x/1.2 NA water immersion lens. A 5μm (unless stated differently) scale bar was included in a representative image of all IF analysis. For the quantifications of PCH during cell cycle, 30-50 nuclei was analyzed for each cell cycle stage. In the study of large foci or "Megafoci" in *HP1β*$^{-/-}$ MEFs, 30-50 cells were analyzed to determine number of cells containing these large foci.

Immunoprecipitations and *pull-downs*

Nuclear and whole-cell extracts were prepared according to the Dignam protocol (Dignam et al., 1983) or when indicated, RIPA buffer extraction (DeSeau et al., 1987). Co-immunoprecipitations were performed using FLAG-agarose (Sigma), HA-agarose (Sigma), Myc antibody (Cell Signaling), and Protein G Agarose (Millipore) (Vaquero et al., 2004). Densitometric analysis of the western blots was performed with Quantity One software (Biorad). After washes, bound material was eluted and analyzed by Western blotting. Bound proteins were eluted with either specific peptides or with 0.2M glycine pH 2,3. Immunoprecipitation results were visualized by Western Blot analysis.

FRET, FLIM-FRET and FRAP assays

FRET efficiency was calculated as $[(F_{RFPafter} - F_{RFPbefore})/F_{RFPbefore}]\times100$, where $F_{RFPafter}$ is the fluorescence of donor after bleaching, and $F_{RFPbefore}$ is before bleaching. Moreover, an

additional negative control of FRET was performed to confirm the threshold of these experiments. FRET analysis was also performed between SirT6-EGFP, a chromatin factor that does bind to HP1, and HP1α-RFP. The analysis showed 2.2% FRET between both proteins, very similar to the donor-only control (1.8%) (Figure S4A-B).

FLIM (fluores¬cence lifetime imaging)-FRET was measured by time-correlated single-photon counting (TCSPC) with an inverted multiphoton laser scanning microscope (Leica TCS SP5) equipped with a single-molecule detection platform and single-photon counting electronics (PicoHarp 300, PicoQuant GmbH). Donor (eGFP) two-photon excitation was performed at 950 nm from a Mai Tai Ti:Sapphire laser (Spectra Physics) with a repetition rate of 80 MHz. Photons were detected by a Single Photon Counting Avalanche Photodiodes (SPAD) (PicoQuant). A fluorescence band-pass filter (500–550 nm) limited the detec¬tion to the donor fluorescence only.

Cells were cultured at 37 °C and 5% CO2 in DMEM (Gibco) supplemented with 10% FBS. After 24 h, 1×10^5 cells were seeded on glass-bottomed 3-cm cell culture plates (MatTek) and grown overnight. Cells were transfected with 60µg of donor only (control) or double transfected with 60µg of donor- and 10µg of acceptor-expressing vec¬tors using electroporation standard protocol. Medium was changed to imaging buffer containing no phenol red. eGFP life¬times were measured using a HCX PL APO lambda blue 63x NA 1.4 Oil Objetive. FLIM was performed on ten fields per sample where ROIs were drawn in foci and fluorescent decay curves were analyzed with SymPhoTime software (PicoQuant) on a pixel-by-pixel basis with high spatial resolution. Donor fluorophore lifetimes were fit to two exponential decay curves to calculate the fraction of fluorophores within each pixel that either interact or do not interact with an acceptor. These lifetimes were then mapped by pseudocolor on a pixel-by-pixel basis over the entire image. Mean FRET efficiency values, E, were calculated from E≒ -(tAD/tD) where τDA is the amplitude-weighted mean fluorescence lifetime of the donor (eGFP) in the presence of accep¬tor (RFP). τD is the mean fluorescence lifetime of the donor only sample (eGFP). The following controls were used to establish and validate the FLIM assay. (1) As a negative control, GFP

lifetime was measured in the absence of the acceptor. (2) As a positive control GFP lifetime was measured in the presence of an acceptor (RFP) already known to be closer within 1-10nm to the donor. FLIM image showed a decrease in GFP fluorescence lifetime in presence of RFP.

FRAP experiments were performed as described(Bosch-Presegue et al., 2011). FRAP was performed using a Zeiss LSM 510 Meta confocal microscope (Carl Zeiss, Thornwood, NY) with a C. Apochromat, 63×/1.2 NA, water-immersion objective and equipped with a on-stage incubation chamber set to 37°C, 5% CO_2, and 95% relative humidity. Double normalization (Phair et al., 2004) was then applied to all FRAP experiments. After normalization, relative fluorescence intensities within the bleached area were plotted as a function of time, yielding the raw FRAP recovery curves. The half-life value (defined as the time required to reach half-maximum recovery) was calculated after the recovery curves had been fit to a standard exponential equation using a FRAP calculation macro (K_FRAPcalcV9.ipf, Kota Miura, EMBL, Germany) run with IgorPro 6.1 software (WaveMetrics, Lake Oswego, OR, USA).

DNA methylation assays

Genomic DNA was converted using an EZ DNA Methylation Gold kit (Zymo Research, Orange, CA, USA). Briefly, a minimum of eight single clones were interrogated for each sample and the methylation frequency was calculated in each case. Specific primers were designed using the MethylExpress® program (Applied Biosystems) for bisulfite sequencing to examine the methylation status of particular CG sites covering the candidate genes promoter regions.

HP1 isoform colocalization analysis

For the HP1 isoform colocalization analysis, the three HP1 isoforms were tagged with fluorescent protein (HP1α-RFP, HP1β-YFP, HP1γ-GFP), and expressed in NIH-3T3 cells independently or simultaneously. Cells were then fixed with paraformaldehyde and

mounted with SlowFade Gold antifade media (ThermoFisher). 3D spectral imaging was performed using a Zeiss LSM510 Meta confocal microscope equipped with a C. Apochromat 63x/1.2 NA water immersion lens. Image analysis was performed using Imaris (Bitplane, A.G.) and custom in-house macros. Images were empirically corrected for chromatic shift using reference images of 1µm TetraSpek beads (ThermoFisher) acquired under the same conditions. Whole chromocenter volume was segmented using the combined mean intensity of all three isoforms, and only voxels within the segmented volume were further interrogated. For each of these voxels, the intensity values were normalized, per channel and per chromocenter, to a range of 0-1. The radial position was determined as the fractional distance of each voxel along the line passing through that voxel's closest point on the chromocenter surface and the center of the chromocenter (0-1). These datum were subjected to pairwise correlation analysis (intensity vs. intensity or intensity vs. radial position) using the scipy stats package(Jones et al., 2001), and 2D-histograms were generated using matplotlib(Hunter, 2007).

ChIPseq correlation analysis

The ChipSeq data was downloaded from GEO from the following studies: HP1α GEO:GSM13759 (Bulut-Karslioglu et al., 2014), HP1β GEO:GSM1584767 (Mattout et al., 2015) and H4K20me3 GEO:GSM656527 (Biolodeau and Young, 2010). The data was converted to fastq using SRA tooolkit. A quality test is performed and adapters and overrepresented sequences are removed from the raw reads. Trimmed sequences are then mapped to the mouse genome (build GRCm38/mm10) using bowtie2 v2.0.5 proghram, taking only uniquely aligned reads with no more than 1 mismatch.SAM/BAM files were further processed using SAMTOOLS v0.1.18. Peak calling was perfomed with MACS2 version 2 was performed with default parameters for the all the samples. Finally the regions of subunits HP1 that interact with H4K20me3 were obtained using Bedtools intersectBed v.2.25.0.

Mnase-based compaction assay

2x106 cells from WT and HP1 KO MEFs were washed with PBS and resuspended and incubated on ice for 10min in RSB buffer (Tris 10mM pH 7.5, NaCl 10mM, MgCl2 3mM, Nonidet P40 10%, and protease inhibitors). After centrifugation (1500 rpm for 5 min), the nuclear pellet was resuspended in 300 µl of nuclear buffer (20mM KCl, 20mM Tris-HCl pH 7.5, 70mM NaCl, 3mM de CaCl2, and protease inhibitors). Samples were divided in aliquots (70ul) to perform a timing of MNase digestion, 2U/70ul, (0, 1.5, 3, 5, 10min). The reaction was stopped with 10mM of EDTA and digestion products were separated on 1.5% agarose gel. Southern blot was performed using Hybond-N+ membrane and was incubated with the major satellite probe (5'-GTGAAATATGGCGAGGAAAACT-3') radioactively labeled with [γ32P] (Perkin-Elmer) using T4 kinase reaction. The signal was detected by autoradiography films and the experiments were quantified measuring the intensity with Fiji program. Experiments were performed with three biological replicates. To calculate the linker histone, we performed an average of three measures between the bands from mono/di/trinucleosomes of the last three digestion conditions using ImageJ program. The distance between the different forms was measured and represented as % relative WT cells. A T-student analysis was performed with the data obtained.

Mitotic analysis

Exponentially growing cells were grown on coverslips and fixed in 4% PFA, permeabilized with 0.5% TritonX-100, stained with antibodies raised against CREST and α-tubulin, and counterstained with DAPI. Images were acquired using a LSM510-META confocal microscope. For quantification of aberrant mitosis, images were acquired using a Plan-Apochromat 20x/0.8 NA objective and fields were chosen to contain at least one metaphase, with a minimum of 100 fields analyzed. Figure images of representative metaphase cells were acquired using a C. Apochromat 63x/1.2 NA water objective.

ChIP-reChIP

reChIP experiments were performed as described(Furlan-Magaril et al., 2009). Primers used for the analysis were listed below:

MAJOR SAT	Fwd 5'-TGGAATATGGCGAGAAAACTG-3' Rev 5'-AGGTCCTTCAGTGGGCATTT-3'
LINE-L1 PROMOTER	Fwd 5'- ACTGCGGTACATAGGGAAGC-3' Rev 5'-TGTGATCCACTCACCAGAGG-3'
LINE-L1 ORF2	Fwd 5'-ACCTGGACGAAATGGACAAA-3' Rev 5'-CATCTGGTCCTGGGCTTTT-3'
H19-ICR3	Fwd 5'-GCTGTTATGTGCAACAAGGG-3' Rev 5'-AAGTTGGCAGCATTTGGGC-3'
H19-ICR1	Fwd 5'-CGCAATCGATTTTGCTGCCACC-3' Rev 5'-CTGCAAGGAGACCATGCCC-3'
H19-ICR-1KB	Fwd 5'-CAATGGACGTACACAGAGGTG-3' Rev 5'-GTCCCATCTAGGAGGCAGC-3'
H19-ICR-2KB	Fwd 5'-CCAGGCCCAATGGCTTTCTC-3' Rev 5'-GTCAGTGTTCTATTGCTGTGG-3'

SUPPLEMENTAL REFERENCES

Biolodeau, S., and Young, R. A. (2010). ChIPSeq for H4K20me3. GSE accession: GSE26680.

Bosch-Presegue, L., Raurell-Vila, H., Marazuela-Duque, A., Kane-Goldsmith, N., Valle, A., Oliver, J., Serrano, L., and Vaquero, A. (2011). Stabilization of Suv39H1 by SirT1 is part of oxidative stress response and ensures genome protection. Mol Cell *42*, 210-223.

Bulut-Karslioglu, A., De La Rosa-Velazquez, I. A., Ramirez, F., Barenboim, M., Onishi-Seebacher, M., Arand, J., Galan, C., Winter, G. E., Engist, B., Gerle, B., *et al.* (2014). Suv39h-dependent H3K9me3 marks intact retrotransposons and silences LINE elements in mouse embryonic stem cells. Mol Cell *55*, 277-290.

DeSeau, V., Rosen, N., and Bolen, J. B. (1987). Analysis of pp60c-src tyrosine kinase activity and phosphotyrosyl phosphatase activity in human colon carcinoma and normal human colon mucosal cells. J Cell Biochem *35*, 113-128.

Dignam, J. D., Martin, P. L., Shastry, B. S., and Roeder, R. G. (1983). Eukaryotic gene transcription with purified components. Methods Enzymol *101*, 582-598.

Dryhurst, D., Ishibashi, T., Rose, K. L., Eirin-Lopez, J. M., McDonald, D., Silva-Moreno, B., Veldhoen, N., Helbing, C. C., Hendzel, M. J., Shabanowitz, J., *et al.* (2009). Characterization of the histone H2A.Z-1 and H2A.Z-2 isoforms in vertebrates. BMC Biol *7*, 86.

Furlan-Magaril, M., Rincon-Arano, H., and Recillas-Targa, F. (2009). Sequential chromatin immunoprecipitation protocol: ChIP-reChIP. Methods Mol Biol *543*, 253-266.
Hunter, J. D. (2007). Matplotlib: A 2D Graphics Environment. Computing in Science & Engineering *9*, 90-95.
Jones, E., Oliphant E, and P, P. (2001). Open Source Scientific Tools for Python (http://www.scipy.org).
Kuzmichev, A., Margueron, R., Vaquero, A., Preissner, T. S., Scher, M., Kirmizis, A., Ouyang, X., Brockdorff, N., Abate-Shen, C., Farnham, P., and Reinberg, D. (2005). Composition and histone substrates of polycomb repressive group complexes change during cellular differentiation. Proc Natl Acad Sci U S A *102*, 1859-1864.
Lleres, D., James, J., Swift, S., Norman, D. G., and Lamond, A. I. (2009). Quantitative analysis of chromatin compaction in living cells using FLIM-FRET. J Cell Biol *187*, 481-496.
Mattout, A., Aaronson, Y., Sailaja, B. S., Raghu Ram, E. V., Harikumar, A., Mallm, J. P., Sim, K. H., Nissim-Rafinia, M., Supper, E., Singh, P. B., *et al.* (2015). Heterochromatin Protein 1beta (HP1beta) has distinct functions and distinct nuclear distribution in pluripotent versus differentiated cells. Genome Biol *16*, 213.
Phair, R. D., Gorski, S. A., and Misteli, T. (2004). Measurement of dynamic protein binding to chromatin in vivo, using photobleaching microscopy. Methods Enzymol *375*, 393-414.
Sekimata, M., Perez-Melgosa, M., Miller, S. A., Weinmann, A. S., Sabo, P. J., Sandstrom, R., Dorschner, M. O., Stamatoyannopoulos, J. A., and Wilson, C. B. (2009). CCCTC-binding factor and the transcription factor T-bet orchestrate T helper 1 cell-specific structure and function at the interferon-gamma locus. Immunity *31*, 551-564.
Serrano, L., Liang, L., Chang, Y., Deng, L., Maulion, C., Nguyen, S., and Tischfield, J. A. (2011). Homologous recombination conserves DNA sequence integrity throughout the cell cycle in embryonic stem cells. Stem Cells Dev *20*, 363-374.
Tsang, L. W., Hu, N., and Underhill, D. A. (2010). Comparative analyses of SUV420H1 isoforms and SUV420H2 reveal differences in their cellular localization and effects on myogenic differentiation. PLoS One *5*, e14447.
Vaquero, A., Scher, M., Erdjument-Bromage, H., Tempst, P., Serrano, L., and Reinberg, D. (2007). SIRT1 regulates the histone methyl-transferase SUV39H1 during heterochromatin formation. Nature *450*, 440-444.
Vaquero, A., Scher, M., Lee, D., Erdjument-Bromage, H., Tempst, P., and Reinberg, D. (2004). Human SirT1 interacts with histone H1 and promotes formation of facultative heterochromatin. Mol Cell *16*, 93-105.
Vaquero, A., Scher, M. B., Lee, D. H., Sutton, A., Cheng, H. L., Alt, F. W., Serrano, L., Sternglanz, R., and Reinberg, D. (2006). SirT2 is a histone deacetylase with preference for histone H4 Lys 16 during mitosis. Genes Dev *20*, 1256-1261.
Yu, Y. L., Chou, R. H., Shyu, W. C., Hsieh, S. C., Wu, C. S., Chiang, S. Y., Chang, W. J., Chen, J. N., Tseng, Y. J., Lin, Y. H., *et al.* (2013). Smurf2-mediated degradation of EZH2 enhances neuron differentiation and improves functional recovery after ischaemic stroke. EMBO Mol Med *5*, 531-547.